Energy Conversion and Management 365 (2026) 121694

Contents lists available at ScienceDirect

Energy Conversion and Management

journal homepage: www.elsevier.com/locate/enconman

Research paper

Optical and thermal performance analysis of ceramic foam solar receivers in parabolic dish solar collector assemblies: The role of collector geometrical and optical parameters and absorber and coating materials

Leonardo F. Martins [a], Jorge E.P. Navalho [a,b,c,*], Miguel A.A. Mendes [a], José C.F. Pereira [a]

[a] LAETA, IDMEC, Instituto Superior Técnico, Universidade de Lisboa, Av. Rovisco Pais, 1, 1049-001 Lisbon, Portugal
[b] UNIDEMI, Department of Mechanical and Industrial Engineering, NOVA School of Science and Technology, Universidade NOVA de Lisboa, 2829-516, Caparica, Portugal
[c] Laboratório Associado de Sistemas Inteligentes (LASI), 4800-058, Guimarães, Portugal

ARTICLE INFO

Keywords:
Volumetric solar receiver
Parabolic dish concentrator
Monte Carlo ray tracing
Pore-scale numerical simulation
Ceramic foam
Collector efficiency

ABSTRACT

Volumetric solar receivers perform a critical role in high-efficiency concentrated solar power systems, where effective absorption and conversion of concentrated solar radiation directly determine overall performance. This study presents a fully coupled pore-scale modeling framework that integrates Monte Carlo ray tracing with direct hydrothermal simulations on silicon carbide (SiC) and alumina (Al_2O_3) ceramic foam geometry acquired by computed tomography scans. The approach accurately captures radiative propagation, absorption distribution throughout the porous structure and subsequent fluid flow and heat transfer processes — all without resorting to empirical closure relations.

A detailed parametric analysis examines the influence of parabolic dish concentrator parameters — rim angle, focal length, aperture radius, axial misalignment error and surface slope error — on the spatial distribution of solar flux and angle of incidence at a target probe surface (receiver entrance section). Results show that higher rim angles produce more intense but compact focal spots with wider angular dispersion, while even small misalignments ($\delta_f/f \approx 0.006$–0.008) or surface slope errors rapidly degrade uniformity, increase optical spillage and promote non-uniform heating.

Pore-scale simulations further reveal the impact of these radiation field variations and absorber material choice on receiver performance. Compared to silicon carbide, alumina foams exhibit lower optical efficiency due to poorer absorptivity but superior conversion of absorbed power to useful heat owing to reduced thermal conductivity limiting front-surface losses. Pyromark-coated alumina foam combines high absorptivity with low conductivity, yielding the highest optical and thermal efficiencies, elevated outlet temperatures and enhanced volumetric effect. Findings confirm that stronger volumetric heating does not necessarily improve thermal efficiency and highlight key design trade-offs for optimizing volumetric receivers.

1. Introduction

The IPCC's 6th Assessment Report (2023) states that limiting global warming to a 1.5 °C requires immediate and deep greenhouse gas emission reductions across all sectors [1]. In response to this challenge, a global transition to sustainable energy systems is underway, which is most evident in the power sector [2].

The transition to a low-carbon economy is expected to substantially increase the demand for energy storage to address the intermittency of renewable sources [2]. Concentrating solar power (CSP) systems with thermal energy storage capacity offer a promising solution by storing solar energy as heat and enabling dispatchable electricity generation even at night or during cloudy periods. The CSP systems, such as parabolic dish collector and solar tower systems, use solar receivers to convert concentrated solar radiation into thermal energy [3]. Among the different CSP technologies, parabolic dish collectors are particularly noteworthy as they achieve the highest solar-to-electric conversion efficiency — with a maximum reported value of 31.25% [4] — and high concentration ratios [5]. These systems represent an important research area for high-temperature applications and decentralized energy solutions.

* Corresponding author at: UNIDEMI, Department of Mechanical and Industrial Engineering, NOVA School of Science and Technology, Universidade NOVA de Lisboa, 2829-516, Caparica, Portugal.
E-mail address: jorge.navalho@fct.unl.pt (J.E.P. Navalho).

https://doi.org/10.1016/j.enconman.2026.121694
Received 26 March 2026; Received in revised form 12 May 2026; Accepted 22 May 2026
Available online 4 June 2026

Nomenclature

A_{aper}	Concentrator aperture area, m^2
CR	Flux (optical) concentration ratio, –
CR^*	Normalized flux concentration ratio, –
CR_g	Geometrical concentration ratio, –
f	Concentrator focal length, m
p	Pressure, Pa
q_{gas}	Total power absorbed by the heat transfer fluid, W
q_{rec}^{aper}	Concentrated solar power at the receiver aperture section, W
q_{rec}^{tot}	Total concentrated solar power absorbed by the receiver, W
$q_{rec,loss}$	Radiative power loss from the receiver, W
q_{tot}	Total concentrated solar power, W
q''_c	Concentrated solar flux, $W\,m^{-2}$
q''_s	Solar flux incident on the concentrator surface (direct normal irradiation), $W\,m^{-2}$
r	Radial position on the target probe surface, m
R_{aper}	Concentrator aperture radius, m
r_{core}	Focal spot core radius, m
r_{max}	Focal spot maximum radius, m
T	Temperature, K

Greek symbols

α_{spill}	Optical spillage loss factor, –
ΔT	Temperature difference, K
δ_f	Axial offset value between the target probe surface and the concentrator focal plane, m
ϵ	Emissivity, –
ϵ_{ap}	Apparent emissivity, –
η_{op}	Optical efficiency, –
η_{th}	Thermal efficiency, –
η_o	Overall efficiency, –
Ω	Relative radiative power loss from receiver, –
ω	Solar half-angle, mrad
ψ_{rim}	Concentrator rim angle, °
ρ_{conc}	Concentrator reflectivity, –
σ_s	Surface slope error, mrad
θ_i	Angle of incidence, °

Subscripts

0	centerpoint
avg	average
eff	effective
front	absorber front (irradiated) section
gas	fluid
max	maximum
min	minimum
out	receiver outlet section
rear	absorber rear section
sol	solid
sur	receiver surface
theo	theoretical

Solar receivers suffer from significant heat losses, making improved designs a key research priority. In this sense, volumetric receivers have emerged as particularly promising class, widely applied in focal-point of concentrator systems [3,6]. Current research has explored different porous structures, ranging from random packed beds to highly ordered honeycomb monoliths and open-cell foams [7]. Recent advances even include 3D-printed lattices with gradual porosity, designed to optimize the volumetric effect by tailoring the radiation penetration depth to the local heat transfer requirements [8,9]. Volumetric receivers materials consist of a permeable porous structure — typically ceramic — that allows deep penetration of concentrated solar radiation into its volume (volumetric effect). Ceramics are preferred over metals due to their resistance to oxidising atmospheres, high melting point, low thermal expansion and excellent thermal shock resistance, which make them more suitable for high-temperature applications [10]. In the case of metal foams, the outlet temperatures reach in range 800–1000 °C [6], while in ceramics, such as silicon-infiltrated silicon carbide (SiSiC) or pure silicon carbide (SiC), it is possible to reach a maximum of 1200 °C and 1500 °C [6], respectively.

The absorbed energy is transferred by convection to a heat transfer fluid (HTF) that flows through the porous structure at atmospheric or pressurized conditions. In open volumetric receivers the air is commonly used due to its abundance, negligible global warming potential (GWP) and stability at high temperatures [11,12]. Alternatives such as CO_2 could also be used, as they offer higher heat capacity at elevated temperatures [11]. The high outlet temperature of the HTF allows it to be integrated into industrial process heat supply or conventional thermodynamic cycles (Rankine, Brayton, combined or Stirling), thus replacing fossil-fuel heat sources [3,6,13].

However, achieving optimal thermal performance requires careful selection of the foam's microstructural parameters, as these strongly influence the convective heat transfer between the porous absorber and the HTF. The pore diameter directly affects temperature distribution: smaller pores increase specific surface area [14], thus enhancing thermal efficiency [14,15], but raise pressure losses [16,17] and the risk of local overheating [15]. Higher porosity promotes deeper radiation penetration [18,19], reduces reflection losses [20,21] and improves temperature uniformity [16], which is essential to prevent structural damage. Cell density and strut thickness also determine specific surface area, thereby influencing convective heat transfer and pressure losses [22,23]. Therefore, optimal receiver design requires maximizing solar absorption and heat transfer while simultaneously controlling pressure drop and thermal gradients.

To accurately predict these competing effects and maximize overall performance, the modeling approach must capture both radiative transfer and fluid flow within the porous structure.

For this purpose, two main approaches have been suggested in the literature: the surface approach and the volumetric effect approach [3]. While the surface approach considers absorption only at the front section of the receiver, the volumetric effect approach more accurately reflects the physical phenomenon, by accounting for the penetration and continuous absorption of incident solar radiation throughout the porous structure. The volumetric effect, allows the higher temperatures of the absorber to be moved into the porous matrix, thus preventing energy losses through thermal emission to the surrounding environment and improving energy conversion efficiency [3,8,16].

The most common volumetric approach has been applied through the modified P1 approximation [24–27], the discrete ordinates method [28,29] or through exponential laws [20,30]. Alternatively, the volumetric approach using Monte Carlo ray tracing (MCRT) techniques can be implemented in a fully coupled procedure that directly tracks radiation from the solar disk to the within walls of the receiver.

Radiative heat transfer within porous media has been extensively investigated using MCRT approaches, which resolve radiation interactions with solid domain at the pore-scale. Several studies [31–33], have demonstrated that radiation propagates through the void phase until it encounters the solid matrix, where it undergoes partial absorption and reflection — commonly modeled using specular or diffuse approaches — leading to multiple successive interactions. This framework enables the characterization of absorption, scattering, and transmission phenomena arising from the complex morphology of porous structures. The modeling of detailed porous geometries in MCRT involves not only a trade-off between accuracy and computational cost, but also significant challenges associated with the explicit representation of highly complex pore-scale structures. To address this, voxel-based MCRT algorithms [34] discretize the domain into a binary (solid/void) grid, bypassing complex surface reconstruction and simplifying ray–geometry interactions to efficient sequential voxel stepping. This approach avoids intensive intersection tests and achieving speed-ups of approximately 90 times, while maintaining close agreement with classical MCRT results. Alternatively, when pore-scale resolution is too costly, stochastic radiation models [35] and equivalent porous media approximations [10,36] — volume-averaging and continuum approaches — are used, representing the structure as a participating medium rather than deterministic surfaces. However, these macroscopic models require the estimation of effective properties [32,37], which capture the underlying pore-scale physics.

Modeling volumetric receivers involves two interconnected aspects: first, the absorption of solar radiation within the porous structure [38,39], and second, the coupling of this radiation absorption with fluid flow [10,36]. This coupling is typically achieved by modeling solar radiation absorption separately — commonly using MCRT methods — and then incorporating it as a heat source term in the energy conservation equation.

Indeed, the absorption of radiation in porous media is a complex problem due to the interaction between the morphological characteristics of the intricate porous structure and its optical properties. To address this challenge, numerous studies have been applied in literature, ranging from 1D continuous models [40–43] to fully distributed and discrete 3D models at pore-scale [18,21,44,45]. However, the most common modeling approach has been based on the formulation of local thermal non-equilibrium (LTNE) with 2D or 3D volume averaging [10,30,36,46,47].

The continuum models include a source term in the momentum conservation equation that represents the effect of the porous media and this term depends on the geometry of the porous material and fluid flow conditions [10,47].

In case of local thermal equilibrium approach, only a single energy equation is used for both phases, which means that the fluid and solid temperatures are the same at each location (is equivalent to assume an infinite convective heat transfer coefficient [42,48]) and the effect of high temperature gradient at the front surface of the volumetric absorber are neglected.

Whereas the local thermal non-equilibrium approach solves at least two coupled energy equations, one per phase. The heat transfer rates between solid and fluid phases dominates the energy transport in porous media and these strongly rely on the application of external correlations for the evaluation of convection heat transfer coefficients [3,24,49]. The convection heat transfer coefficient significantly affects the accuracy of the theoretical model under LTNE conditions [30] and, at same time, several conflicting correlations have been proposed in the literature to represent them, but each of these has limitations [24].

In contrast, the pore-scale simulation solves the continuity, momentum and energy equations directly within the reconstructed geometry — typically obtained via X-ray computed tomography. By resolving all transport mechanisms within the microstructure, this framework eliminates the need for external empirical correlations [3,45] — such as prescribed heat transfer coefficients, permeability correlations and extinction coefficients —, allowing effective properties to emerge naturally from the fully resolved pore-scale solution. Although computationally demanding, pore-scale methods provide detailed physical insights when properly coupled with accurate radiative transfer modeling.

In this sense, some studies have applied pore-scale modeling approaches to investigate the complex thermo-fluid processes occurring within porous volumetric solar receivers. These works have focused on resolving the coupled mechanisms of radiative, conductive, and convective transport within the porous absorber, thus providing detailed insights into the interaction between the solid structure and the heat transfer fluid [18,21,50]. Based on this detailed physical description, pore-scale simulations have also been used to analyze how the morphological characteristics of the foam — such as pore size, porosity, and structural topology — influence key performance indicators, including pressure losses, temperature distribution, and overall thermal efficiency of volumetric receivers [22,51]. Other studies have employed tomography-based reconstructed geometries to derive macroscopic correlations, such as Nusselt number correlations, and to assess the impact of geometrical parameters on convective heat transfer [52]. These developments have also made it possible to evaluate the validity of conventional continuum approaches, thereby revealing the limitations of the volume-averaging models — widely applied in the literature — for predicting receiver performance [53].

At the same time, some investigations have extended pore-scale analyses to include the role of optical properties and radiation absorption within the intricate porous absorber. Some of them analyzing different strategies to control optical properties in order to enhance energy absorption and overall efficiency [29,45]. In addition, experimentally validated pore-scale studies have demonstrated that these approaches are capable of accurately predicting the behaviour of high-temperature and high-efficiency volumetric solar receivers [54].

This work applies a fully coupled modeling framework to characterize the performance of a parabolic dish solar collector equipped with an open volumetric ceramic foam receiver. This approach directly integrates surface heat source (power per surface) distributions — obtained from MCRT — with fully resolved pore-scale conjugate heat transfer simulations performed on real ceramic foam geometry acquired by computed tomography scans. In this study, solar flux distributions predicted through MCRT are consistently mapped onto a 3D discrete representation of the foam, enabling detailed hydrothermal simulations that resolve the complex solid–fluid interactions within the porous structure. A dedicated data management strategy is implemented to ensure coherent and accurate coupling between the optical and hydrothermal models while addressing the intrinsic morphological complexity of the receiver.

Extending our previous work [3], a comprehensive parametric analysis is performed to assess the influence of key concentrator parameters — including rim angle, focal length, aperture radius, axial receiver misalignment, and surface slope errors — on the spatial distributions of solar flux and incidence angle at the focal plane. These geometrical and optical parameters are tested to characterize the optical, thermal, and global efficiencies of the different receiver systems, while a novel perspective is proposed to characterize the volumetric effect. Finally, the performance of different absorber materials, such as silicon carbide and alumina, is compared alongside the benefits of applying selective coatings.

The paper is organized as follows. Section 2 describes the physical model of the parabolic dish concentrating solar collector, including the receiver geometry and solar resource characterization. Sections 3 and 4 details the mathematical and numerical models, covering the coupled Monte Carlo ray tracing and pore-scale hydrothermal models, along with boundary conditions, thermophysical properties and optical assumptions. Section 5 presents and discusses the results: first, the influence of concentrator geometrical and optical parameters on solar flux and incidence angle distributions; second, a comprehensive parametric study evaluating the effects of these parameters and absorber material variations on overall receiver optical and thermal performance. Finally, Section 6 summarizes the main findings and provides recommendations for future volumetric receiver design improvements.

2. Physical model — concentrating solar collector

Fig. 1 illustrates the concentrating solar collector physical model considered in this study. The full collector model is composed by the concentrating solar collector system and the solar model. The collector system is composed by two main components: the parabolic dish concentrator and the volumetric solar receiver. The parabolic dish harnesses and redirects direct solar radiation to a small focal region where the receiver front (irradiated) section is located. The volumetric solar receiver absorbs the solar radiation provided and augmented by the parabolic dish and transfers the corresponding energy by a forced convection regime to a heat transfer fluid that is provided at the receiver front section.

The parabolic dish geometry is fully defined by stating two of the following parameters: focal length (f), aperture radius (R_{aper}), and rim angle (ψ_{rim}). These parameters are related with each other according to Eq. (1) [55,56].

$$\frac{f}{R_{\mathrm{aper}}} = \frac{1}{2\tan\left(\frac{\psi_{\mathrm{rim}}}{2}\right)} \tag{1}$$

Additionally, the optical (and thermal) performance of a parabolic dish collector is dependent on other parameters, such as the concentrator surface slope error, alignment errors between the parabolic dish and the receiver front section — axial offset (δ_f) —, reflectivity of the absorber structure surface (absorber material and coating) and housing structure. (Other parameters also play a role in the overall collector performance namely the concentrator surface reflectivity, the dimensions of the receiver aperture section in relation to the geometrical and optical parameters of the parabolic dish, the reflectivity of the tubular housing structure, the absorber internal pore structure, the location of the absorber structure in tubular housing structure.)

Fig. 2 presents the physical model of the volumetric solar receiver unit. The volumetric solar receiver is comprised by a ceramic open-cell porous foam cylindrical absorber structure, the heat transfer fluid (atmospheric air) — that flows through the intricate internal porous foam structure — and a tubular housing structure where the absorber is fixed to confine the heat transfer fluid. The diameter and length of the absorber structure are equal to 25 mm and 20 mm, respectively, and consistent with laboratory-scale receivers commonly used in experimental validation studies. Its geometrical characteristics, listed in Table 1, are representative of commercially available ceramic foams employed in high-temperature volumetric receiver applications. (The reconstruction process of this foam structure from a real sample is reported elsewhere [57].) The tubular housing structure is 30 cm long

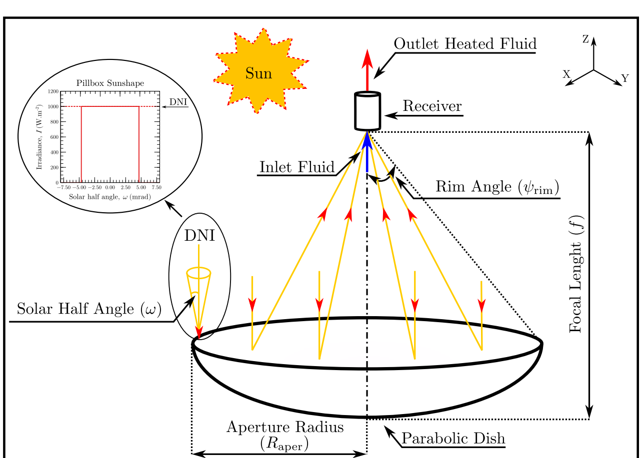

Fig. 1. Schematic representation of the concentrating solar collector physical model.

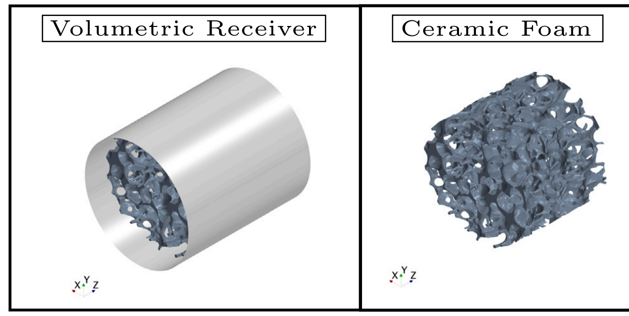

Fig. 2. Physical model of the volumetric solar receiver unit.

Table 1
Geometrical parameters of the open-cell foam solar absorber.

Parameter	Value
Cell density, n (ppi)	10
Porosity, ϕ (%)	83
Specific surface area, a_V ($\mathrm{m^{-1}}$)	669
Strut diameter, d_{strut} (mm)	0.7
Pore diameter, d_{pore} (mm)	4.8

and holds the absorber in place at the middle of the structure — the absorber front section is 5 mm distant from the tubular opening section (receiver front section). The thickness of the tubular housing structure is neglected.

The solar flux model adopted in this work assumes a pillbox distribution according to which the solar radiative intensity is uniform across the solar cone with an half-angle equal (ω) to 4.65 mrad [58]. The solar half-angle determines the degree of collimation of the incident direct solar rays. Different values for the direct normal irradiation (DNI) are considered in this study with the value of 1000 W m^{-2} being considered the reference. (DNI quantifies the intensity of beam solar radiation measured perpendicular to the direction of propagation of solar rays.)

3. Mathematical models

The receiver thermal performance evaluation is obtained through the solution of the receiver hydrothermal model. The receiver hydrothermal model solution requires the concentrated solar heat flux distribution on the surface of the receiver internal porous structure. The concentrated solar heat flux distribution within the receiver structure is computed in the framework of the collector solar flux (optical) model taking into account the solar model characteristics and geometrical and optical parameters of the solar collector system. Moreover, the collector solar flux model application allows to evaluate the collector optical performance. The collector solar flux and receiver hydrothermal mathematical models are described in this section.

3.1. Collector solar flux model

The solar flux model uses the Monte Carlo ray tracing method, widely applied in concentrated solar energy research. The method employs individual tracking of a large number of rays coming from the solar disk. Rays undergo reflection on the concentrator surface until they are either absorbed by the receiver or escape the domain. Upon hitting a particular collector surface, absorption or reflection is determined stochastically based on local optical properties and a random number generator [59,60].

3.2. Receiver hydrothermal model

The receiver hydrothermal model is comprised by a set of fluid flow and energy governing equations that are solved directly in the reconstructed discrete three-dimensional porous receiver geometry. The current receiver model does not require and rely on unsuitable externally-derived correlations and effective thermophysical properties and geometrical parameters as the widely applied volume-averaging modeling approach. Highly reliable receiver hydrothermal performance characterization is expected with direct pore-scale models. The primary constraint on the widespread application of this class of models is the need for detailed acquisition and digital reconstruction of the porous geometry, together with the high computational cost of solving the governing mathematical equations.

3.2.1. Governing equations

The steady-state governing equations, derived under the assumptions of laminar flow, and negligible body forces and volumetric energy sources, are presented in Eqs. (2)–(5). These equations correspond, respectively, to the continuity equation, the momentum balance equation, and the energy conservation equations for the fluid and solid domains.

$$\nabla \cdot (\rho \mathbf{v}) = 0 \tag{2}$$

$$\nabla \cdot (\rho \mathbf{v} \otimes \mathbf{v}) = \nabla \cdot \boldsymbol{\sigma} \tag{3}$$

$$\nabla \cdot (\rho E \mathbf{v}) = \nabla \cdot (\mathbf{v} \cdot \boldsymbol{\sigma}) - \nabla \cdot (-k_{\mathrm{gas}} \nabla T_{\mathrm{gas}}) \tag{4}$$

$$\nabla \cdot (-k_{\mathrm{sol}} \nabla T_{\mathrm{sol}}) = 0 \tag{5}$$

In these equations, ρ, $\mathbf{v}$, $\boldsymbol{\sigma}$, E, k, and T are the fluid density, velocity vector, stress tensor, total fluid energy per unit mass, thermal conductivity, and temperature, respectively. The subscripts gas and sol refer to the receiver gaseous and solid phases, respectively. The stress tensor is defined in Eq. (6), where p denotes the pressure and $\mathbf{T}$ the viscous stress tensor, as given by Eq. (7), with μ representing the dynamic viscosity of the fluid.

$$\boldsymbol{\sigma} = -p\mathbf{I} + \mathbf{T} \tag{6}$$

$$\mathbf{T} = \mu[\nabla \mathbf{v} + (\nabla \mathbf{v})^T] - \frac{2}{3}(\nabla \cdot \mathbf{v})\mathbf{I} \tag{7}$$

The total fluid energy per unit mass is related with the fluid specific enthalpy (h) according to Eq. (8).

$$E = h + \frac{1}{2}\|\mathbf{v}\|^2 - \frac{p}{\rho} \tag{8}$$

Air within the receiver void (pore) volume is assumed to be transparent [61] (non-participating) in radiative heat transfer — the receiver heat transfer fluid neither emits, absorbs, nor scatters radiation [49,61]. Accordingly, the net radiation (surface-to-surface) method [62] is used to compute the net radiative heat flux between receiver surfaces and the external environment.

3.2.2. Thermophysical properties

Temperature-dependent thermophysical properties are considered due to the large temperature range expected in the receiver operation. Air density is calculated by applying the ideal gas law — see Eq. (9), where p and T correspond to the absolute pressure (Pa) and temperature (K), respectively.

$$\rho\left(\mathrm{kg\,m^{-3}}\right) = \frac{p}{287.04\,T_{\mathrm{gas}}} \tag{9}$$

Air dynamic viscosity is evaluated by using Sutherland's law that is given by Eq. (10), with fluid temperature expressed in kelvins [63].

$$\mu\left(\mathrm{kg\,m^{-1}\,s^{-1}}\right) = \frac{1.4535 \times 10^{-6} T_{\mathrm{gas}}^{1.5}}{T_{\mathrm{gas}} + 110.4} \tag{10}$$

Air specific heat and thermal conductivity at atmospheric pressure conditions are evaluated with Eqs. (11) and (12), respectively, where temperatures are expressed in kelvins [3]. These equations are valid over the temperature range 250–1600 K.

$$\begin{aligned} c_p\left(\mathrm{J\,kg^{-1}\,K^{-1}}\right) = {} & 2.4422 \times 10^{-10} T_{\mathrm{gas}}^4 - 9.6767 \times 10^{-7} T_{\mathrm{gas}}^3 + \\ & 1.3251 \times 10^{-3} T_{\mathrm{gas}}^2 - 5.3090 \times 10^{-1} T_{\mathrm{gas}} + 1.0703 \times 10^3 \end{aligned} \tag{11}$$

$$\begin{aligned} k_{\mathrm{gas}}\left(\mathrm{W\,m^{-1}\,K^{-1}}\right) = {} & 3.4288 \times 10^{-11} T_{\mathrm{gas}}^3 - 9.1803 \times 10^{-8} T_{\mathrm{gas}}^2 + \\ & 1.2940 \times 10^{-4} T_{\mathrm{gas}} - 5.2076 \times 10^{-3} \end{aligned} \tag{12}$$

The absorber thermal conductivity is evaluated with Eq. (13) and Eq. (14) depending on the actual absorber material under consideration — silicon carbide (SiC) and alumina (Al_2O_3), respectively — and considering temperatures given in degrees Celsius. The thermal conductivity correlations for SiC and Al_2O_3 presented in Eq. (13) and Eq. (14) were derived experimentally and are valid along the temperature range of 0–2000 °C [64] and 20–1800 °C [65], respectively.

$$k_{\mathrm{sol}}\ (\mathrm{W\,m^{-1}\,K^{-1}}) = \frac{52000 \times \exp(-1.24 \times 10^{-5} T_{\mathrm{sol}})}{T_{\mathrm{sol}} + 437} \tag{13}$$

$$k_{\mathrm{sol}}\ (\mathrm{W\,m^{-1}\,K^{-1}}) = 5.85 + \frac{15360 \times \exp(-0.002 T_{\mathrm{sol}})}{T_{\mathrm{sol}} + 516} \tag{14}$$

3.2.3. Boundary and interface conditions

The computational domain of the receiver hydrothermal model is bounded by the inlet section, outlet section, and lateral wall. The computational model inlet (outlet) section is extended $0.5D$ ($3D$) upstream (downstream) the physical inlet (outlet) section presented in Section 2 — D corresponds to the diameter of the receiver external (lateral) surface. The additional fluid region upstream the absorber (foam) front section acts as a fluid entrance (developing) region to avoid the application of unsuitable (non-physical) fluid inlet conditions near the absorber front section. The additional fluid region downstream the absorber structure is required to avoid velocity and pressure fluctuations and backflow issues in the numerical solution.

At the inlet section of the computational domain, uniform velocity and temperature distributions are imposed — equal to $0.1\,\mathrm{m\,s^{-1}}$ and $300\,\mathrm{K}$, respectively. At the outlet section, zero gauge pressure is imposed and fully developed temperature profiles (negligible axial temperature gradient) is assumed. (Atmospheric pressure corresponds to the reference temperature.) No-slip and impermeable boundary conditions are applied to the velocity field and the receiver internal surfaces — interface between the heat transfer fluid and the absorber and receiver lateral wall. Moreover, the receiver lateral wall (cylindrical surface) is adiabatic — heat transfer is not observed through the receiver lateral surface towards the receiver external region. (The lateral wall of the extruded (additional) inlet fluid region does not correspond to a physical surface. Accordingly, slip (frictionless) and adiabatic boundary conditions are applied, and the wall is treated as radiatively transparent (transmissivity equal to one) to allow radiative heat transfer between the receiver and the surrounding surfaces.) For the heat transfer fluid at direct contact with the receiver tubular (lateral) surface, a second-type (Neumann) boundary condition is applied — see Eq. (15). In Eq. (15), $\mathbf{n}$ is the boundary unit normal vector and q''_{ext} and q''_{int} correspond, respectively, to the concentrated solar radiation flux — determined in the framework of the solar collector model — and thermal (long-wave) radiation exchange within the receiver and between the receiver components and the surrounding environment.

$$\left(k_{\mathrm{gas}} \nabla T_{\mathrm{gas}} \cdot \mathbf{n}\right) + q''_{\mathrm{ext}} + q''_{\mathrm{int}} = 0 \tag{15}$$

At the interface between the heat transfer fluid and the absorber solid region, conjugate heat transfer conditions given by Eqs. (16) and (17) are considered.

$$\left(k_{\mathrm{sol}} \nabla T_{\mathrm{sol}} \cdot \mathbf{n}\right) = q''_{\mathrm{ext}} + q''_{\mathrm{int}} + \left(k_{\mathrm{gas}} \nabla T_{\mathrm{gas}} \cdot \mathbf{n}\right) \tag{16}$$

$$T_{\mathrm{gas}} = T_{\mathrm{sol}} \tag{17}$$

3.3. Optical and radiative properties

All collector surfaces are modeled as opaque, gray [3] and with wavelength-independent properties. Under this set of assumptions, Kirchhoff's law of thermal radiation establishing that the total hemispherical solar absorptivity (α) is equal to the total hemispherical thermal emissivity (ϵ) [62].

Although the emissivity of silicon carbide foam can vary in range 0.93–0.96 [11], a value of 0.93 was adopted for this study, which is in agreement with the results presented in the literature [3]. Regarding to emissivity of alumina foam it was set to 0.65 — well-below the corresponding value of 0.93 for SiC. The emissivity of alumina was calculated with the expression reported in Ref. [66] for a temperature of $1000\,\mathrm{K}$ (about the average solid temperature expected during operation).

The emissivity of the outer surface of the receiver structure was set at 0.30. This value aligns with parameters typically employed in previous studies [3,26,36], and represents a low-emissivity surface to mitigate radiation losses to the surrounding environment.

Unless otherwise stated, the concentrator surface reflectivity (ρ_{conc}) was set at 0.90 [3,36,42,67] and it has been assumed to be independent of incidence angle. This assumption, which is valid for specular reflection, is consistent with approaches adopted in previous studies [33,61, 68,69].

4. Numerical models

4.1. Collector solar flux model

The open-source MCRT software Tonatiuh is applied for calculating the solar irradiation absorbed by the collector surfaces. The procedure employed for computing the absorbed solar flux distribution on the irradiated receiver surfaces was previously described and validated in Ref. [3], where a detailed ray-number independence analysis was conducted by comparing simulations with increasing numbers of traced rays against a reference solution obtained with 100 million rays. This analysis demonstrated that, for 80 million rays, the relative error in the total absorbed solar power on the receiver surfaces was approximately 0.006%, while the maximum local distribution error along the absorber axial direction remained below 5%, with the highest deviations confined to regions subjected to negligible absorbed solar flux near the absorber outlet section.

The reliability of the MCRT approach adopted in this study was established in Ref. [3] by comparing the obtained flux distributions and flux concentration ratio against theoretical benchmark data. The results showed that the model accurately captures the spatial distribution and peak concentration ratios, providing a validated optical input for subsequent hydrothermal model simulations.

The grid-mapping strategy adopted in the present work follows the same approach detailed in Ref. [3], wherein each boundary cell face of the pore-scale fluid flow and heat transfer model is geometrically associated with a specific surface element in the MCRT model, guaranteeing a consistent and conservative transfer of heat flux distributions between the optical and hydrothermal models. This one-to-one correspondence between the optical and CFD (computational fluid dynamic) meshes avoids the need for interpolation schemes and ensures the spatial coherence of the coupled framework.

4.2. Receiver hydrothermal model

The receiver mathematical model is numerically solved through the commercial software STAR-CCM+. The integrated CAD modeling functionalities of the software are used for both mesh generation and computational domain discretization.

The governing Navier–Stokes equations are solved using the built-in segregated flow solver based on the SIMPLE algorithm. The energy conservation equation is solved with a segregated solver to determine the temperature distribution in the fluid phase, employing second-order upwind spatial discretization for convective terms. The heat transfer between fluid and solid phases in the porous receiver structure is handled through a conjugate heat transfer formulation. This approach is essential as it accounts for the distinct governing equations of each phase while simultaneously computing temperature and heat flux distributions at the phase interfaces without the need for externally specified convection coefficients.

The net radiation method available in STAR-CCM+ is used to account for thermal radiation heat transfer. View factors are calculated using a deterministic Monte Carlo approach based on ray tracing, and a ray-number independence analysis was performed to ensure the accuracy of the computed view factors. The radiation and energy equations are iteratively coupled until both temperature and radiative source terms converge below specified tolerances — all residuals falling below a threshold of 1×10^{-6} —, ensuring a consistent treatment of the large temperature gradients arising within the porous structure.

A mesh independence study was also conducted for the pore-scale simulations to guarantee that the numerical results are independent of the spatial discretization. As detailed in Ref. [3], the adopted refinement level ensures a high geometrical accuracy, with relative errors for porosity and specific surface area below 0.15%. Furthermore, the mesh convergence analysis for the hydrodynamic behavior showed that mean and maximum velocity magnitude errors remained below 0.012% and 0.070%, respectively. It is important to emphasize that all reported relative errors were calculated using the results from the most refined mesh case (comprising about 32 million cells) as the reference. These results confirm that the selected mesh resolution provides an accurate representation of the ceramic foam's complex structure and fully resolves the flow field and thermal gradients. Additional details can be found elsewhere [3].

Regarding the reliability of the CFD approach, the close agreement observed in Ref. [3] for both hydrodynamic and thermal parameters against reference data reinforces the suitability of pore-scale model predictions.

5. Results and discussion

The effect of parabolic dish collector geometrical and optical parameters are investigated at two different levels: firstly, at the receiver aperture section level in Section 5.1; and secondly, at the receiver whole-system level in Section 5.2. Moreover, at the receiver whole-system level the effect of different absorber ceramic materials and the application of a high-solar absorptivity coating is investigated (Section 5.2). At the receiver aperture section the distribution of concentrated solar flux and angle of incidence is analyzed in detail. At the receiver system level, the concentrated solar flux is analyzed on the internal absorber porous surface as well as the gas and solid temperatures and integral performance parameters such as optical, thermal and overall efficiencies.

5.1. Role of concentrator parameters on the concentrated solar flux and incident angle distributions at the receiver aperture section

In order to investigate the role of parabolic dish collector geometrical and optical parameters on the distribution of concentrated solar flux and angle of incidence, a target probe disk surface was employed. The target probe disk surface has a radius of $2.5\times10^{-2}\,R_{\mathrm{aper}}$ and was uniformly discretized along the radial direction with 50 annular disks each one defined by an inner radius and outer radius — resulting in a radial spacing of $5\times10^{-4}\,R_{\mathrm{aper}}$. The probe surface is normal to and centered on the parabolic dish symmetry axis and is located at a specified distance (δ_f) from the concentrator focal plane. The geometry of the parabolic dish concentrator is fully defined by stating two of the following parameters: focal length (f), aperture radius (R_{aper}), and rim angle (ψ_{rim}). The distance between the probe surface and the parabolic dish focal plane (δ_f) — axial alignment error — and the concentrator surface slope error (σ_s) are important sources of geometrical and optical errors in concentrating solar collector systems. Axial alignment errors may result from prolonged (long-term) collector operation or improper installation. The slope error of a concentrator surface leads to angular deviations from the specular reflection direction due to local geometrical imperfections of the concentrator surface caused by manufacturing and installation processes.

The angle of incidence of an individual ray striking on the target probe surface is computed according to Eq. (18), where $\vec{n}$ and $\vec{v}_j$ are unit vectors normal to the probe surface and collinear with the ray path between the concentrator and the probe surface (defined towards the concentrator), respectively. For each control annular disk surface, the resulting angle of incidence (θ_i) is the average of the angle of incidence for all rays striking the control annular disk surface.

$$\theta_{i,j} = \cos^{-1}\left(\vec{v}_j \cdot \vec{n}\right) \tag{18}$$

For the current conditions, dimensional analysis shows that the local flux (optical) concentration ratio (concentrated solar flux normalized by the solar heat flux, $CR \equiv q''_c/q''_s$) and the local incident angle are functions of the following four non-dimensional groups: r/R_{aper}, ψ_{rim} (or R_{aper}/f), σ_s, and δ_f/f.

For the parametric analysis presented in this section (Section 5.1), the dish surface is considered a perfectly reflective surface — ideal surface with no absorption losses ($\rho = 1$) — with no geometrical defects. In Section 5.1.1, to investigate the role of geometrical dish parameters (f, R_{aper}, and ψ_{rim}), the probe surface is placed at the concentrator focal plane and no concentrator optical (non-specular reflection) errors are considered — *i.e.*, $\delta_f = 0$ and $\sigma_s = 0$. For different rim angles, the effect of the surface slope error is investigated at the focal plane ($\delta_f = 0$) in Section 5.1.2 and the effect of the axial alignment error is investigated neglecting the surface slope error ($\sigma_s = 0$) in Section 5.1.3.

5.1.1. Effect of concentrator geometrical parameters

For different parabolic dish rim angles, Figs. 3(a) and 3(b) present the profiles of normalized (flux) concentration ratio ($CR^* \equiv CR/CR(r=0)$) and angle of incidence, respectively, as a function of radial position normalized by the aperture radius ($r/R_{\text{aper}} \equiv r^*_{\text{aper}}$) and focal length ($r/f \equiv r^*_f$). These profiles reveal how the concentrated solar radiation and angle of incidence vary from the center to the periphery of the target probe surface.

In Figs. 3(a) and 3(b), normalized concentration ratio and incident angle profiles exhibit a characteristic pattern with the corresponding focal spots at the target probe surface consisting of two regions: (i) a central core region ($r \le r_{\text{core}}$), where the normalized concentration ratio and incident angle are uniform — equal to about 1 and $\theta_{i,\min}$, respectively; and (ii) a peripheral (tail) region ($r_{\text{core}} < r \le r_{\max}$) characterized by a sharp normalized concentration ratio drop to zero and an incident angle increase to a maximum value ($\theta_{i,\max}$).

Fig. 4(a) presents the radius of the focal spot core region (r_{core}) and the maximum radius of the focal spot ($r_{\max}$) normalized by the parabolic dish aperture radius and focal length for different rim angles. Fig. 4(b) show the centerpoint concentration ratio ($CR(r=0)$) and minimum, maximum and average angles of incidence ($\theta_{i,\min}$, $\theta_{i,\max}$, and $\theta_{i,\text{avg}}$) for different rim angles. (The average incident angle is defined as a weighted mean of the local incident angles with the local normalized concentration ratios — $\theta_{i,\text{avg}} \equiv \int_A \theta_i CR^* dA / \int_A CR^* dA$.)The values presented in Figs. 4(a) and 4(b) were obtained with MCRT simulations and based on theoretical calculations — according to Eqs. (19)–(22) adapted from [70]. Particularly, Eq. (22) was obtained neglecting shadowing effects by the probe surface on the concentrator surface.

$$\left(\frac{r_{\text{core}}}{f}\right)_{\text{theo}} = \tan(\omega) \tag{19}$$

$$\left(\frac{r_{\max}}{f}\right)_{\text{theo}} = \frac{2\tan(\omega)}{(1+\cos(\psi_{\text{rim}}))\cos(\psi_{\text{rim}})} \tag{20}$$

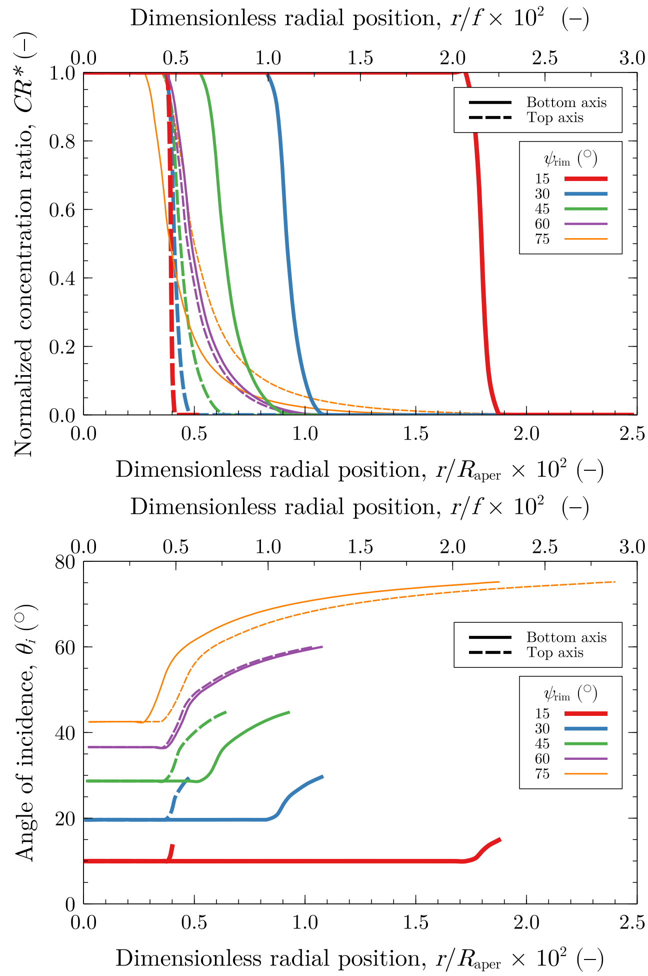

Fig. 3. Normalized concentration ratio profiles (a) and incident angle profiles (b) along the target probe surface radial direction normalized by the parabolic dish aperture radius (bottom axis) and focal length (top axis). No optical and geometrical errors are considered — $\sigma_s = 0$ and $\delta_f = 0$.

$$CR_{\text{theo}}(r=0) = \frac{\sin^2(\psi_{\text{rim}})}{\tan^2(\omega)} \tag{21}$$

$$\left(\theta_{i,\min}\right)_{\text{theo}} \equiv \theta_{i,\text{theo}}(r=0) = \frac{\sin(2\psi_{\text{rim}}) - 2\psi_{\text{rim}}\cos(2\psi_{\text{rim}})}{4 - 4\cos^2(\psi_{\text{rim}})} \tag{22}$$

Figs. 3(a)–3(b) and 4(a) show that as the parabolic dish rim angle increases, the central core radius (r_{core}) and the maximum focal spot radius ($r_{\max}$) vary differently depending whether the rim angle increase is being promoted by a decrease in the focal length or an increase in the aperture radius — see Eq. (1). If the rim angle increase is being supported by a decrease of the focal length (constant R_{aper}), the central core radius decreases — $r_{\text{core}}/R_{\text{aper}}$ decreases upon increasing ψ_{rim} — while the maximum focal spot radius decreases for low rim angles to 45° — but less sharply than $r_{\text{core}}/R_{\text{aper}}$ — and then increases. Thus, for a particular concentrator aperture radius, the geometrical concentration ratio observed without optical spillage ($CR_g^{\text{NoSpill}} \equiv A_{\text{aper}}/A_{\text{focal spot}} = R^2_{\text{aper}}/r^2_{\max}$) is maximum — approximately equal to 11562.030 — for a rim angle equal to 45°. On the other hand, if the rim angle increase is being supported by an increase of the aperture radius (constant f), the central core radius remains constant — $r_{\text{core}}/f \approx 5 \times 10^{-3}$ — while the maximum focal spot radius increases monotonically with the rim angle. In any case, as the concentrator rim angle increases — as the focal length decreases or the aperture radius increases —, the extent of the focal spot peripheral (tail) region ($r_{\max} - r_{\text{core}}$) increases continuously.

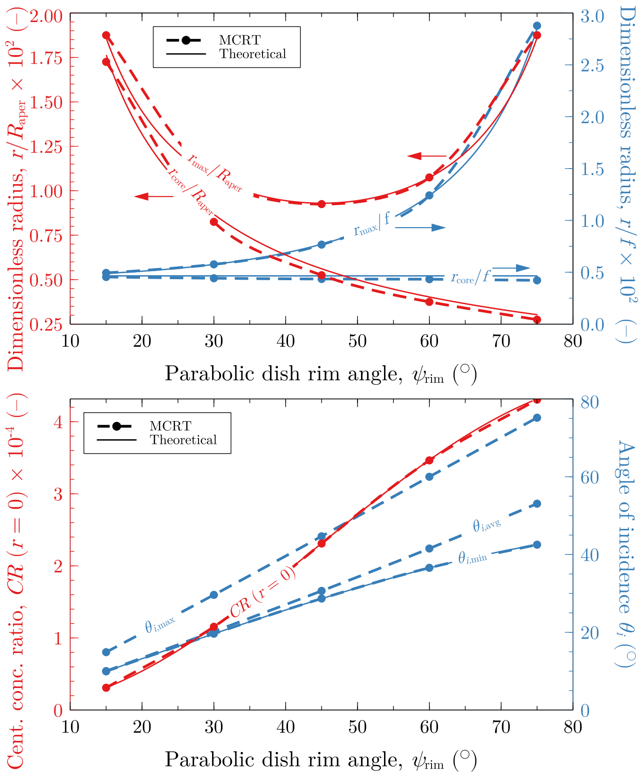

Fig. 4. Focal spot core and focal spot maximum dimensionless radius (a) and centerpoint concentration ratio and minimum, maximum, and average incident angles (b) for different rim angles. No optical and geometrical errors are considered — $\sigma_s = 0$ and $\delta_f = 0$.

Consequently, the transition from high to low heat flux values spans over a wider radial distance, resulting in smoother profiles. Moreover, the fraction of the total power reflected by the concentrator that hits the focal spot core region (q_{core}/q_{tot}) increases as the rim angle decreases — for instance, this fraction is about 56% and 87% for a rim angle equal to 60° and 30°, respectively.

Fig. 4(b) shows that the centerpoint concentration ratio increases with the concentrator rim angle. If the rim angle increase is achieved by increasing the aperture radius the total power at the target probe surface (q_{tot}) increases — see Eq. (23), where both the centerpoint concentration ratio and the integral increase with the aperture radius according to Figs. 3(a) and 4(b).

$$q_{tot} = 2\pi q_s'' CR(r=0) \int_0^{r_{max}} CR^* r dr \tag{23}$$

Alternatively, if the rim angle increase is obtained by reducing the focal length, the total power at the target probe surface remains constant — the increase observed in the centerpoint concentration ratio is compensated by a decrease in the integral of Eq. (23). Therefore, the total power at the target probe surface is fully dictated by the concentrator aperture area taking into account that spillage losses and solar radiation blockage effects are negligible. (Shadowing losses are estimated less than 0.1% of the total power that would be harvested by an unblocked concentrator based on the ratio between the areas of the probe surface and concentrator surface.)

Figs. 3(b) and 4(b) show that the minimum, maximum and average incident angles are determined by the concentrator rim angle. As the concentrator rim angle increases, the local incident angles also increase. Particularly, the maximum incident angle increases at a higher pace with the rim angle than the minimum and average incident angles. Consequently, the difference between the minimum and maximum incident angles also increases with the rim angle. The maximum incident angle — observed at the edge of the focal spot ($r = r_{max}$) — corresponds to about the rim angle. For low rim angles (below about 30°), the average incident angle is approximately equal to the minimum incident angle — this evidence is observed because the fraction of the total power hitting the focal spot tail region is low and the maximum incident angles are not significantly different than the minimum incident angles.

For higher rim angle values, the concentrator surface becomes more curved and deeper and the concentrator areas furthest from the center have a steeper angles of inclination, which forces the rays to converge towards the probe surface from wider angles. Consequently, rays hit the target probe surface with a much great angular dispersion and the local incident angles increase. However, for lower rim angle values, the concentrator has a smaller curvature (flatter geometry) and the rays reflected from the concentrator surface follow trajectories that are approximately parallel to the concentrator axis, and consequently, incident angles at the probe surface are smaller. Therefore, for lower rim angles the concentrated solar radiation becomes more perpendicular to the focal plane and the collimated incident radiation (CIR) assumption — broadly applied in the literature [21,36,71,72] — becomes more suitable.

5.1.2. Effect of surface slope error

For different (and typical) concentrator surface slope error values, Figs. 5(a) and 5(b) present the profiles of normalized concentration ratio and angle of incidence, respectively, as a function of the dimensionless radial position (r/R_{aper}) while Fig. 6 presents the concentration ratio at the center of the target probe surface and the minimum, maximum, and average incident angles.

In these figures, three concentrator rim angle values (30°, 45°, and 60°) are considered and geometrical errors — such as axial misalignment of the probe surface in relation to the concentrator focal plane ($\delta_f \neq 0$) — are negligible. For the three rim angles, as the surface slope error increases, the focal spot core region — within which CR^* and θ_i are constant — vanishes. The focal spot core region becomes negligible for a surface slope error greater or approximately equal to 1 mrad — this evidence is particularly noticeable in the normalized concentration ratio profiles. An increase in the surface slope error leads to a smoother and more gradual drop of the normalized concentration ratio profiles along the radial direction as well as an increase in the irradiated area — r_{core} decreases rapidly towards zero and r_{max} increases progressively. Therefore, an increase in the surface slope error has a significantly negative impact on the concentrator performance. Such an increase in r_{max} upon increasing the surface slope error inevitably leads to optical spillage losses for a target probe surface of reduced dimensions — for the target probe surface dimensions under consideration and a surface slope error of 4 mrad, the optical spillage loss factor account to 32.6%, 11.3%, and 7.4% for a rim angle of 30°, 45°, and 60°, respectively. (The optical spillage loss factor corresponds to the fraction of the power reflected by the concentrator that is lost by spillage from the receiver aperture section.) For fixed target probe surface dimensions and concentrator surface slope error, existent spillage losses tend to increase as the concentrator rim angle decreases. As the surface slope error is increased the centerpoint concentration ratio decreases — such decrease is particularly remarkable from 1 to 3 mrad (see Fig. 6). This evidence is in line with the fact that the total power provided by the concentrator is constant for a particular concentrator aperture radius and r_{max} (or focal spot total area) increases with the surface slope error. (The surface slope error is responsible for scattering the reflected solar radiation over a larger focal spot region at the cost of a decrease of the local concentration ratios at the inner focal spot region.) Moreover, the relevance of the actual rim angle value on the centerpoint concentration ratio becomes lower for higher surface slope error values — note in Fig. 6 that the difference between the centerpoint concentration ratios for the three rim angles under consideration decreases as the surface slope error increases.

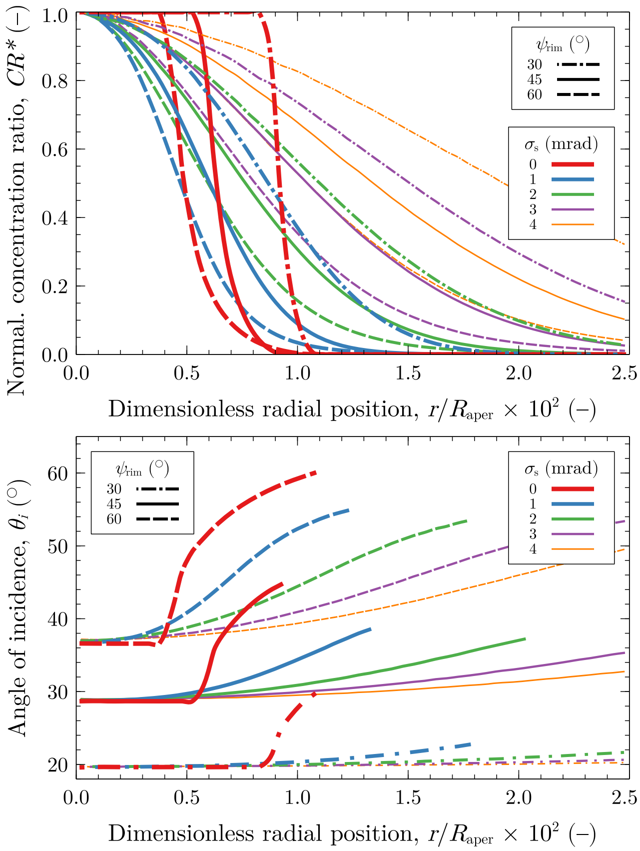

Fig. 5. Normalized concentration ratio profiles (a) and incident angle profiles (b) along the target probe surface dimensionless radial direction for three concentrator rim angles and different concentrator surface slope error values. No geometrical errors are considered — $\delta_f = 0$. Incident angle profiles (Figure (b)) are plotted over the normalized flux concentration ratio of $1 \geq CR^* \geq \max\left(0.01, CR^*\left(r^*_{aper} = 2.5 \times 10^{-2}\right)\right)$.

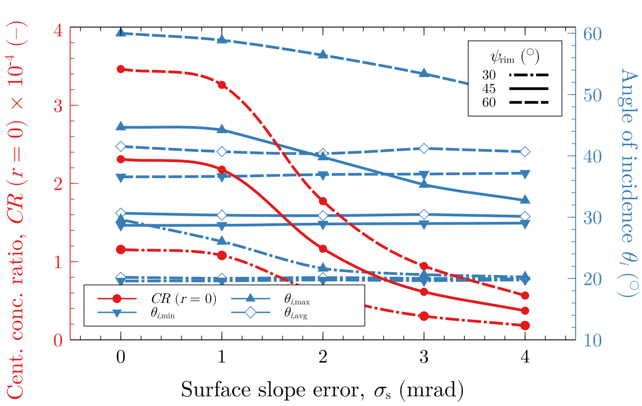

Fig. 6. Centerpoint concentration ratio and minimum, maximum, and average incident angles for three concentrator rim angles and different concentrator surface slope error values. No geometrical errors are considered — $\delta_f = 0$. Average incident angles computed over the normalized flux concentration ratio of $1 \geq CR^* \geq \max\left(0.01, CR^*\left(r^*_{aper} = 2.5 \times 10^{-2}\right)\right)$.

Figs. 5(b) and 6 show that as the surface slope error increases, the minimum incident angle (centerpoint incident angle) increases marginally whereas the maximum incident angle — observed at the edge of the focal spot ($r = r_{max}$) — shows a pronounced decline. The slight increase in the minimum incident angle arises because larger surface slope errors cause peripheral regions of the concentrator to contribute to the radiation intercepted at the center of the target probe surface. As a result, the incident angle profiles become more uniform (flatter) upon increasing the surface slope error, since the difference between the maximum and minimum incident angles decrease. (For a rim angle of 45°, the incident angle profiles range from 28.7° to 44.7° for the perfectly specular reflective surface condition and from 29.0° to 32.7° for a surface slope error equal to 4 mrad.) Moreover, for a given surface slope error, lower rim angles result in a smaller difference between the maximum and minimum incident angles — considering a surface slope error of 4 mrad, the difference between $\theta_{i,max}$ and $\theta_{i,min}$ is about 0.5°, 3.7°, and 12.3° for a rim angle equal to 30°, 45°, and 60°, respectively (see Fig. 6). For the cases with negligible spillage losses — cases with high rim angles and low surface slope errors — the average incident angle show a slight decrease with the surface slope error.

5.1.3. Effect of axial alignment error

The effect of axial misalignment between the concentrator focal plane and the location of the target probe surface is herein investigated considering different axial offset values nondimensionalized by the concentrator focal length (δ_f/f) for three different concentrator rim angles (30°, 45°, and 60°). Figs. 7(a) and 7(b) present the profiles of normalized concentration ratio and angle of incidence, respectively, as a function of the dimensionless radial position (r/R_{aper}) while Fig. 8 presents the concentration ratio at the centerpoint of the target probe surface and the centerpoint, maximum, and average incident angles. For the rim angles considered in Figs. 7(a)–7(b) and 8, positive and negative dimensionless axial offset values of equal magnitude ($\pm\delta_f/f$) produced similar results. (A positive (negative) axial offset corresponds to an axial displacement of the target probe surface away from (towards) the concentrator along the optical axis.)

As the dimensionless axial offset value increases, the focal spot core region shrinks and the focal spot tail and total regions extend over a larger area — *i.e.*, r_{core}/R_{aper} decreases and r_{max}/R_{aper} increases. For each concentrator rim angle, the focal spot core region vanishes ($r_{core}/R_{aper} \to 0$) for the (critical) dimensionless axial offset value from which the centerpoint concentration ratio begins to drop — see Fig. 8 according to which the centerpoint concentration ratio features a very modest but consistent increase upon increasing the dimensionless axial offset value and then shows a pronounced decrease above the critical value. (The critical value corresponds to the dimensionless axial offset value for which the centerpoint concentration ratio is maximum.) The critical value separates a moderate defocusing regime — observed for low dimensionless axial offset values — from a severe dispersion regime with residual concentration that is registered for high offset values. Moreover, Fig. 8 shows that the critical dimensionless axial offset value increases as the rim angle decreases — the focal spot core region is preserved over a larger axial offset range for lower concentrator rim angles. Therefore, in Figs. 7(a) and 7(b), the focal spot core region is not observed for dimensionless axial offset values equal or above 8×10^{-3} at rim angles of 45° and 60°, and equal or above 12×10^{-3} at the lowest rim angle considered. In fact, Fig. 8 indicates that the critical dimensionless axial offset value lies in the range 6–7 $\times10^{-3}$ and 7–8$\times10^{-3}$ for rim angles of 60° and 45°, respectively, and at approximately 10×10^{-3} for a rim angle equal to 30°.

The slight increase of the centerpoint concentration ratio that is observed as the dimensionless axial offset value is increased up to the critical value (see Fig. 8) suggests that the optimal position for the target probe surface to maximize solar flux concentration is not at the concentrator focal plane. This is because the determination of the geometrical concentrator focal plane does not take into account the effect of the solar half-angle. The actual solar concentration ratio distribution is influenced by the finite angular extent of the solar disk which justifies the observed deviation between the ideal geometrical focus and the position that effectively maximizes the concentration

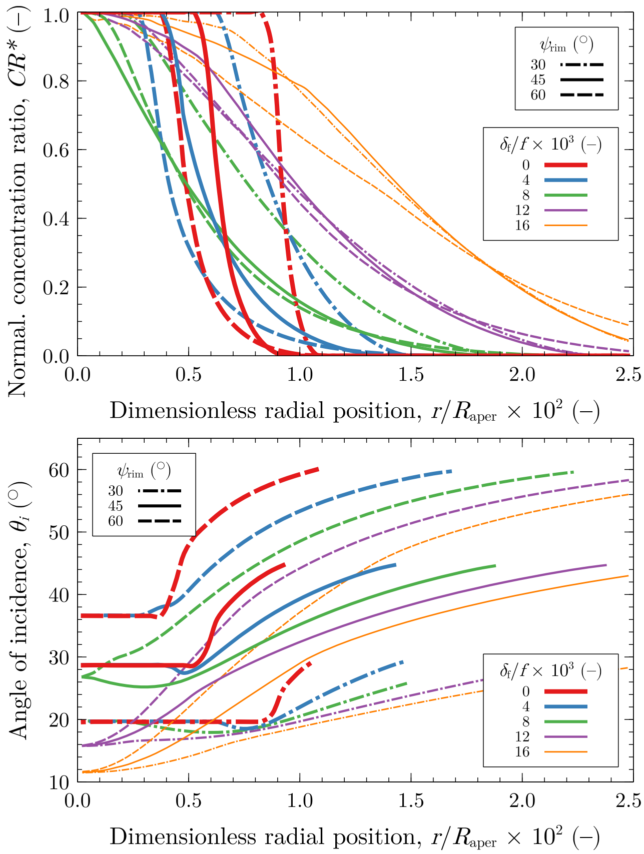

Fig. 7. Normalized concentration ratio profiles (a) and incident angle profiles (b) along the target probe surface dimensionless radial direction for three concentrator rim angles and different dimensionless axial offset values of the target plane. No optical errors are considered — $\sigma_s = 0$.

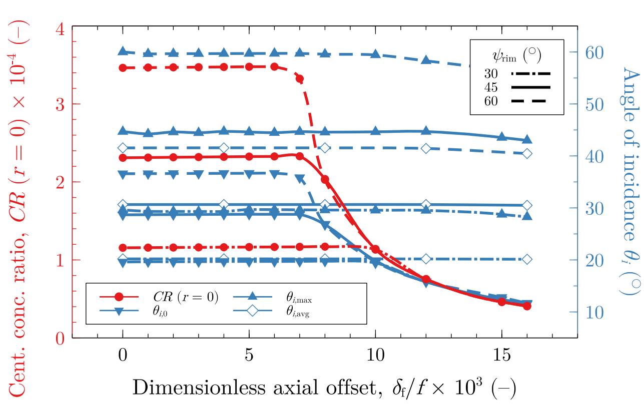

Fig. 8. Centerpoint concentration ratio and centerpoint, maximum, and average incident angles for three concentrator rim angles and different dimensionless axial offset values of the target plane. No optical errors are considered — $\sigma_s = 0$.

ratio. The increase in the centerpoint concentration ratio — in relation to the value observed with negligible axial misalignment error — upon increasing the dimensionless axial offset value is more pronounced for lower concentrator rim angles.

Fig. 8 shows that above the critical dimensionless axial offset value the centerpoint concentration ratio profiles for different rim angles merge into a single profile meaning that the centerpoint concentration ratio becomes independent of the actual rim angle value. A similar conclusion is drawn from Figs. 7(b) and 8 for the centerpoint incident angle: above the critical value the centerpoint incident angle becomes independent of the actual rim angle value and the centerpoint incident angle profiles merge into a single descending curve with the dimensionless axial offset. The centerpoint incident angle decreases with the dimensionless axial offset value because the centerpoint of the target surface becomes unreachable by rays from outer regions of the parabolic dish — rays that would contribute to an increase in the centerpoint incident angle. Fig. 7(b) shows that for small to medium rim angle values, as the dimensionless axial offset value is increased a local minimum incident angle begins to be registered at the edge of the focal spot core region ($r \approx r_{\mathrm{core}}$) and progresses towards the target probe surface centerpoint. For dimensionless axial offset values higher or equal to the critical value, local angles of incidence decrease consistently upon increasing the dimensionless axial offset and the minimum incident angle is observed (exclusively) at the centerpoint of the target surface.

The maximum incident angle — that is consistently observed at the edge of the focal spot region ($r = r_{\max}$) — shows a slight decrease with the dimensionless axial offset due to optical spillage. Since increasing the dimensionless axial offset value the minimum incident angles decreases at a higher rate than the maximum incident angle, the difference between the maximum and minimum incident angles increase with the dimensionless axial offset value. The average incident angle is independent of the dimensionless axial offset value as long as optical spillage losses are negligible because it is dictated by the concentrator geometry (rim angle) and the orientation between the concentrator focal plane and surface target plane — that has been held constant (parallel) in this study.

While no significant differences were observed in the previous results (Figs. 7(a)–7(b) and 8) computed with positive and negative dimensionless axial offset values of equal magnitude (not shown), this symmetry does not hold for all rim angle values. Fig. 9 presents normalized absorbed power profiles for different rim angles as a function of the dimensionless axial offset magnitude for positive and negative axial offset values.

For large rim angles, normalized absorbed power profiles corresponding to negative and positive axial offset values remain nearly overlapping even for relatively large δ_f/f magnitude values, indicating a reduced sensitivity to the axial misalignment direction. As the rim angle decreases, the profiles tend to overlap only for very small δ_f/f magnitude values, showing an approximately symmetric response in this range in relation to the concentrator focal plane — see Fig. 9. However, as δ_f/f increases for smaller rim angles, this overlap progressively vanishes, and the asymmetry becomes more pronounced. In

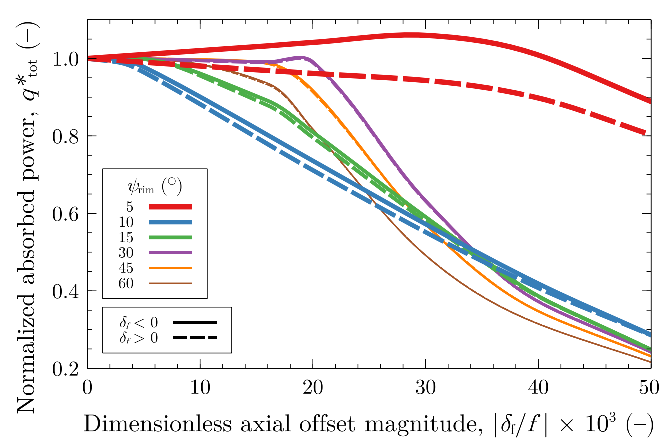

Fig. 9. Normalized absorbed power ($q^*_{\mathrm{tot}} \equiv (q_{\mathrm{tot}})_{\delta_f \neq 0} / (q_{\mathrm{tot}})_{\delta_f = 0}$) on a target probe disk surface of radius equal to $2.5 \times 10^{-2} R_{\mathrm{aper}}$ for different rim angles and positive and negative dimensionless axial offset values.

particular, negative offset values systematically yield higher normalized absorbed power values compared to the positive offset values for the same dimensionless axial offset magnitude, indicating that moving the receiver towards the concentrator is less penalizing in terms of power loss by spillage than shifting it beyond the focal plane.

The asymmetric behaviour observed for the absorbed power at two equal target probe surfaces that are equally distant from the concentrator focal plane but in opposite directions is due to the effect of the solar half-angle. (If the incident radiation were strictly aligned with the concentrator axis — negligible half-angle (collimated radiation) — such asymmetric behaviour would not be observed and absorbed power profiles for positive and negative axial offset values for the same rim angle would overlap with each other.) Furthermore, profiles corresponding to positive (or negative) dimensionless axial offsets become similar for comparable values of the solar half-angle to rim-angle ratio ($\omega/\psi_{\mathrm{rim}}$), as this ratio represents an additional governing dimensionless parameter that quantifies the relative importance of optical and geometrical contributions in determining the concentrator performance. As the ratio $\omega/\psi_{\mathrm{rim}}$ increases (similarly, as the rim angle decreases for a constant solar half-angle), differences in the absorbed power between positive and negative axial offset of equal magnitude become more pronounced. Contrarily, for large rim angles (low $\omega/\psi_{\mathrm{rim}}$ ratios) the geometrical scale clearly dominates the optical behaviour, rendering the contribution associated with a non-negligible solar half-angle relatively secondary in defining the flux distribution at the target probe surface.

5.2. Role of concentrating solar collector parameters and materials on collector optical and receiver hydrothermal performance

In order to evaluate the role of collector geometrical and optical parameters and absorber and coating materials on the collector performance, a reference collector system is herein adopted. The reference collector system is defined by a concentrator aperture radius of 0.2 m and a focal length of 3 m. The concentrator reflectivity is set to 0.9, while surface slope and axial alignment errors are assumed to be negligible. The absorber consists of an uncoated SiC foam structure.

According to Table 2, the effect of the concentrator focal length, concentrator aperture radius, concentrator surface slope error, and collector axial alignment error can be assessed by comparing the results of systems A, B, C, D and E, respectively, against the results of the reference system. The effect of the absorber material and coating application can be investigated with the results of systems F, G, and H and the results of the reference system.

For each collector system comprising a change in a particular geometrical or optical collector parameter in relation to the reference system, two solar system sets are defined: collector–solar systems Y-1 and Y-2, where Y is any of the systems A, B, C, D, and E. For systems Y-1, a particular solar flux value (DNI) at the concentrator surface (q_s'') is defined in such a way that the total absorbed power by the receiver unit ($q_{\mathrm{rec}}^{\mathrm{tot}}$) matches the value registered for the reference case. Consequently, any performance difference observed between System Y-1 and the reference configuration can be attributed exclusively to variations in the concentrated solar flux distribution and the incident angle distribution at the receiver aperture section. For Systems Y-2, the same solar flux value at the concentrator aperture as that considered for the reference system ($1000\,\mathrm{W\,m^{-2}}$) is applied. Therefore, the performance of Systems Y-2 becomes simultaneously dependent on the distributions of concentrated solar flux and incident angle at the receiver aperture as well as on the total absorbed power by the receiver unit.

Regarding the absorber materials, besides uncoated SiC foam considered for the reference system, uncoated Al_2O_3 foam, and Pyromark-coated Al_2O_3 and SiC foams were considered — see collector systems F, G, and H, respectively, in Table 2. The thermal conductivity of alumina is lower than that of silicon carbide (about 71% and 78% lower at 300 and 1300 K, respectively). The emissivity of Al_2O_3 for calculations was set equal to 0.65 — well-below the corresponding value of 0.93 for SiC. Due to the Al_2O_3 low solar absorptivity, a highly absorptive Pyromark paint is commonly applied onto the walls of Al_2O_3 solar absorbers [73]. The emissivity of the Pyromark paint corresponds to 0.95 [73]. The thickness of the paint layer is neglected and, consequently, the absorber pore (void) volume and the intrinsic solid thermal conductivity of the foam are equal to the values of the reference case scenario.

5.2.1. Receiver optical performance

Optical results are presented in Figs. 10–12. For each collector–solar system under consideration, Fig. 10 presents the concentrated solar flux distribution on absorber walls normalized by the maximum observed flux value for each system.

Figs. 11 and 12 present optical performance parameters — optical spillage loss factor, apparent emissivity, optical efficiency, and the relative contribution of three different receiver surface sets on the receiver total absorbed concentrated solar power. The optical spillage loss factor, apparent emissivity, and optical efficiency are evaluated with Eqs. (24), (25), and (26), respectively. (In the absence of relevant optical transmission and shadow losses, the optical efficiency is also given by the product $\rho_{\mathrm{conc}}\left(1-\alpha_{\mathrm{spill}}\right)\epsilon_{\mathrm{ap}}$.)

$$\alpha_{\mathrm{spill}} = 1 - \frac{q_{\mathrm{rec}}^{\mathrm{aper}}}{\rho_{\mathrm{conc}}\, q_s''\, A_{\mathrm{aper}}} \tag{24}$$

$$\epsilon_{\mathrm{ap}} = \frac{q_{\mathrm{rec}}^{\mathrm{tot}}}{q_{\mathrm{rec}}^{\mathrm{aper}}} \tag{25}$$

Table 2
Collector geometrical and optical parameters, absorber materials and coatings, and direct normal irradiance considered for different system. Collector–solar system 1 corresponds to the reference system for the current investigation.

	Collector and solar systems													
	1 (Ref.)	2 (A-1)	3 (A-2)	4 (B-1)	5 (B-2)	6 (C-1)	7 (C-2)	8 (D-1)	9 (D-2)	10 (E-1)	11 (E-2)	12 (F)	13 (G)	14 (H)
Collector														
Conc. focal length, f (m)	3.0	**1.0**	**1.0**	3.0	3.0	3.0	3.0	3.0	3.0	3.0	3.0	3.0	3.0	3.0
Conc. aperture radius, R_{aper} (m)	0.2	0.2	0.2	**0.8**	**0.25**	0.2	0.2	0.2	0.2	0.2	0.2	0.2	0.2	0.2
Conc. surface slope error, σ_s (mrad)	—	—	—	—	—	**2**	**2**	—	—	—	—	—	—	—
Collec. axial alignment error, δ_f/f (−)	—	—	—	—	—	—	—	**−0.05**	**−0.05**	**+0.05**	**+0.05**	—	—	—
Receiver														
Absorber material	SiC	SiC	SiC	SiC	SiC	SiC	SiC	SiC	SiC	SiC	SiC	Al_2O_3	Al_2O_3	SiC
Absorber coating	—	—	—	—	—	—	—	—	—	—	—	—	Pyromark	Pyromark
Solar System														
DNI, q_s'' ($\mathrm{W\,m^{-2}}$)	1000	*803.69*	1000	*64.37*	1000	*2447.63*	1000	*1262.30*	1000	*1383.65*	1000	1000	1000	1000

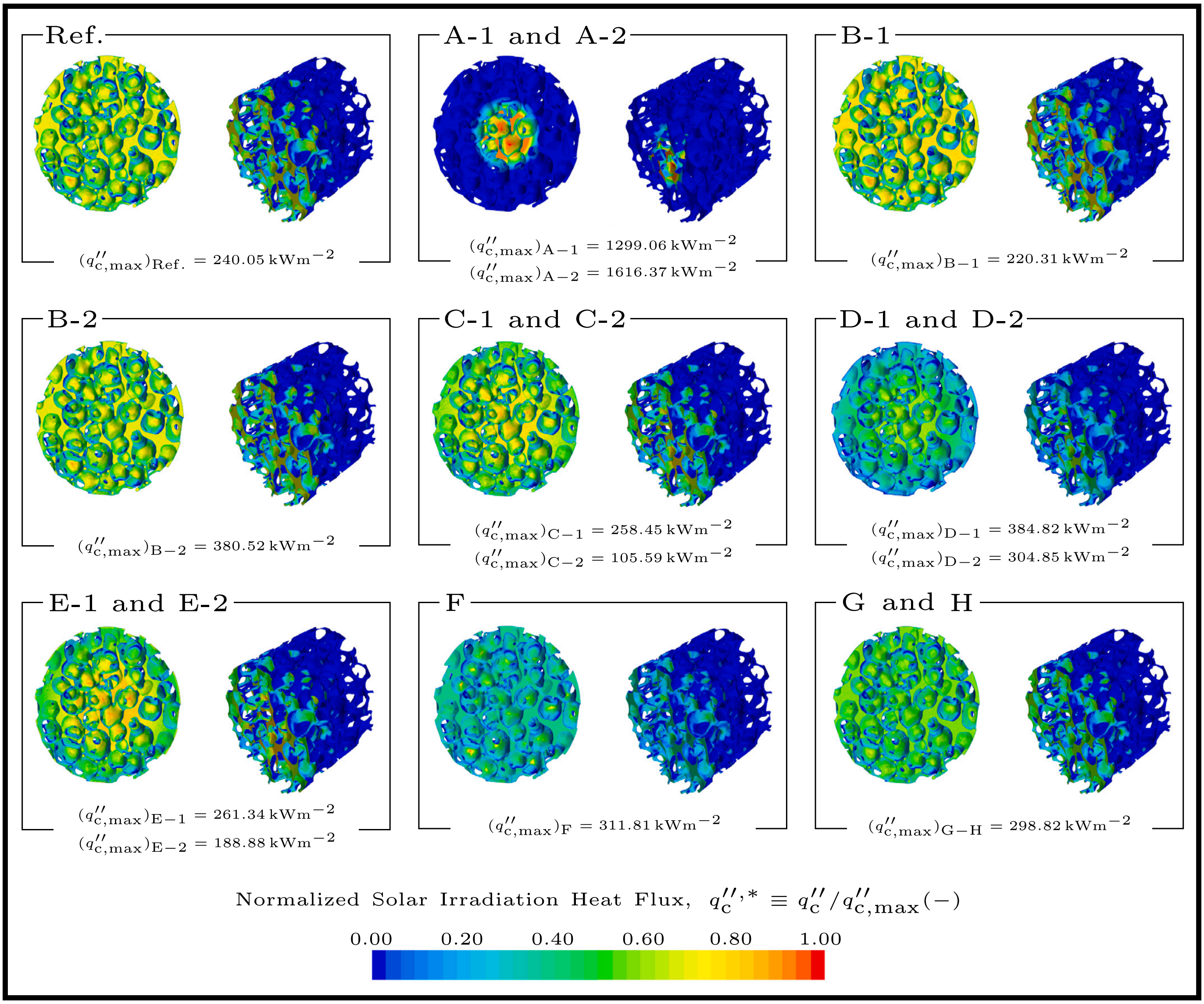

Fig. 10. Normalized concentrated solar flux distribution on the absorber walls.

$$\eta_{\text{op}} = \frac{q_{\text{rec}}^{\text{tot}}}{q_s'' A_{\text{aper}}} \tag{26}$$

In these equations, $q_{\text{rec}}^{\text{aper}}$ and $q_{\text{rec}}^{\text{tot}}$ correspond to the total concentrated solar power at the receiver aperture section (receiver power-on-aperture) and the total concentrated solar power absorbed by the receiver unit, respectively.

The optical performance parameters are independent of the incident solar flux irradiation value at the concentrator aperture which is in full agreement with previous studies (see Ref. [67]). Therefore, optical performance results presented in Figs. 11 and 12 for Systems Y-1 are equally valid for Systems Y-2 — *i.e.*, both systems have the same optical performance. (An exception is observed for systems B-1 and B-2, as they do not share identical geometrical parameters.)

Fig. 11 shows that a significant decrease of the concentrator focal length — by a factor of 3 (from the reference system to system A-1) — improves the optical efficiency, while an increase in the aperture radius, surface slope error or axial alignment error results in a deterioration of the optical efficiency. For such changes in collector parameters in relation to the reference values, the optical efficiency reveals to be mainly susceptible to optical spillage losses — note in Fig. 11 that

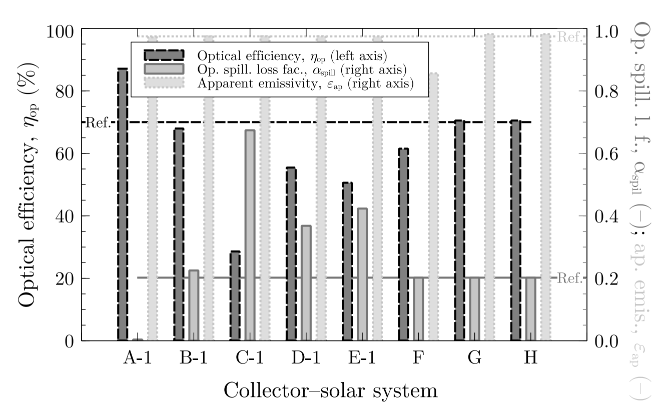

Fig. 11. Optical efficiency, optical spillage loss factor, and apparent emissivity.

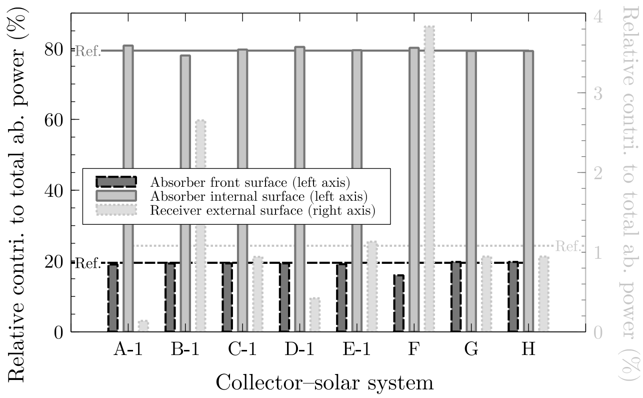

Fig. 12. Contribution of different receiver surfaces to the total absorbed solar power.

for each system the variation of the spillage loss factor in relation to the reference system supports the variation of the optical efficiency in accordance, while the apparent emissivity — that controls reflection losses from the receiver unit — remains almost constant and, consequently, with no significant influence on the optical efficiency change. The effect of each varied optical and geometrical parameter on the optical spillage loss factor is in full agreement with the corresponding effect of each parameter on the concentrated solar flux distribution at the receiver aperture section observed in Section 5.1. Since spillage losses are insignificant for system A-1 — as expected according to the corresponding concentrated solar flux distribution on the absorber walls (see Fig. 10 —, its optical efficiency ($\eta_{\rm op} \approx 87.1\%$) becomes limited by the optical reflection performance of the concentrator surface ($\rho_{\rm conc} = 0.9$) and the apparent absorption characteristics of the receiver surfaces ($\epsilon_{\rm ap} \approx 97.2\%$). (Optical transmission losses were found negligible for all systems due to the absorber high extinction volume — this is in line with a negligible concentrated solar flux observed for all absorber structures particularly near their rear sections in Fig. 10.) The results for systems with axial alignment errors (Systems D and E) show that positive and negative axial offset values of equal magnitude in relation to the concentrator focal plane lead to different (asymmetric) receiver power-on-aperture values which is fully consistent with results presented in Section 5.1.3 — receiver power-on-aperture is higher for System D (negative axial offset value) for which the optical spillage loss factor is lower in relation to System E. The similar apparent emissivity value observed independently of the collector geometrical and optical parameters (concentrator focal length, aperture radius, and surface slope error and collector axial alignment error) means that the shape of the concentrated solar flux and incident angle distributions at the receiver aperture does not play a significant role on the ratio between the total absorbed power and receiver power-on-aperture. Nevertheless, it is worth noting that owing to the highly complex and intricate absorber porous structure, the receiver aperture apparent emissivity for the reference system and systems A-1 to E-1 (approximately equal to 0.975) is higher than the intrinsic SiC surface emissivity which supports the solar radiation entrapment effect.

Although systems A-1 to E-1 were devised to absorb the same total solar power at the receiver unit, Fig. 12 shows that the contribution of each set of receiver surfaces to absorb solar radiation is not equal for every system. This evidence demonstrates that the contribution of each receiver surface set to the total absorbed power becomes dependent on the shape of the radial solar flux profile and direction distribution of incident solar beams at the receiver aperture. Independently of the system under consideration, the absorption of concentrated solar power is predominantly observed at the absorber internal surfaces — *ca.* 78.0%–80.8% of the total power absorption takes place in the internal absorber volume. The concentrated solar power absorbed at the receiver tubular surface accounts for the lowest share — about 0.1%–3.8%. Due to the characteristics of the concentrated solar flux and incident angle distributions at the receiver aperture for System A-1 (the focal spot is concentrated at the central region of the absorber), the receiver tubular surface absorbs a negligible fraction (about 0.1%) of the total power. For System B-1, the higher contribution of the lateral wall to the total absorbed power in relation to the corresponding contribution observed for the reference system is justified by the fact that an increase in the concentrator aperture area leads to an increase in the receiver local incident angles — see Section 5.1.1. (The estimated local incident angles for System B-1 are approximately fourfold higher than those associated with the reference parameters while the shape of the solar flux profile at the receiver aperture section is similar for the reference system and System B-1.) For the effect of the surface slope error (system C-1), a similar contribution of each receiver surface collection in absorbing concentrated solar radiation in relation to the reference system is observed. Slight differences are observed between results of Systems D-1 and E-1 even though the distance at which the receiver aperture section is located from the concentrator focal plane are the same. This is in line with the differences reported in Fig. 11 and in Section 5.1.3.

Regarding the optical performance obtained for different absorber and coating materials, Fig. 11 shows that the optical spillage loss factor for Systems F, G, and H is equal to the value observed for the reference system. This is because the optical spillage loss factor is determined by the optical and geometrical features of concentrator and receiver aperture which were held constant for such systems — the optical spillage loss factor is not influenced by optical properties and geometrical characteristics of the receiver internal volume. (Optical spillage and concentrator absorption losses do not play any role in the optical efficiency change that is observed while replacing the absorber material because these losses are accounted for prior (upstream) the solar radiation impingement onto the absorber structure surfaces.) As such, the optical efficiency for Systems F, G, and H varies exclusively due to changes in apparent emissivity. An alumina absorber structure (System F) is incapable of absorbing the same concentrated solar load as a silicon carbide absorber due to its poorer effective optical properties — $\epsilon_{\rm ap}\,({\rm F}) \approx 0.856$ *vs.* $\epsilon_{\rm ap}\,({\rm Ref.}) \approx 0.975$. A Pyromark-coated absorber foam (Systems G or H) features the highest apparent emissivity value — approximately equal to 0.981 which is slightly higher than the value registered for an uncoated SiC foam (0.975) — and, consequently, the highest optical efficiency (70.51%). The highest variation from the intrinsic emissivity to the apparent emissivity value was observed for alumina (0.650 to 0.856) suggesting that the solar radiation entrapment effect is more expressive for lower intrinsic absorber surface emissivities.

Fig. 12 indicates that for an alumina absorber (System F), the fraction of power absorbed at the front absorber surface is lower than that observed for a silicon carbine absorber or a Pyromark-coated absorber. Since reflected radiation from the absorber front section contributes to increase the relevance of the tubular receiver surface, the contribution of the tubular receiver surface to the total absorbed power is expected to be higher for an alumina absorber than for silicon carbine or Pyromark-coated absorbers — see Fig. 12. The internal absorber surfaces play a more relevant relative role in radiation absorption for alumina than for SiC or Pyromark-coated foams. For an alumina absorber, solar radiation absorption takes place over a longer portion of the porous structure due to multiple beam reflections (more reflection events are expected at lower surface emissivities) and the highly complex porous structure that will eventually absorb the radiation but in an extended porous volume.

5.2.2. *Receiver hydrothermal performance*

Combined collector optical and receiver hydrothermal results are presented in Figs. 13–15. Particularly, Figs. 13(a)–(b) present the total absorbed power ($q^{\rm tot}_{\rm rec}$), the relative emission losses (Ω) — fraction

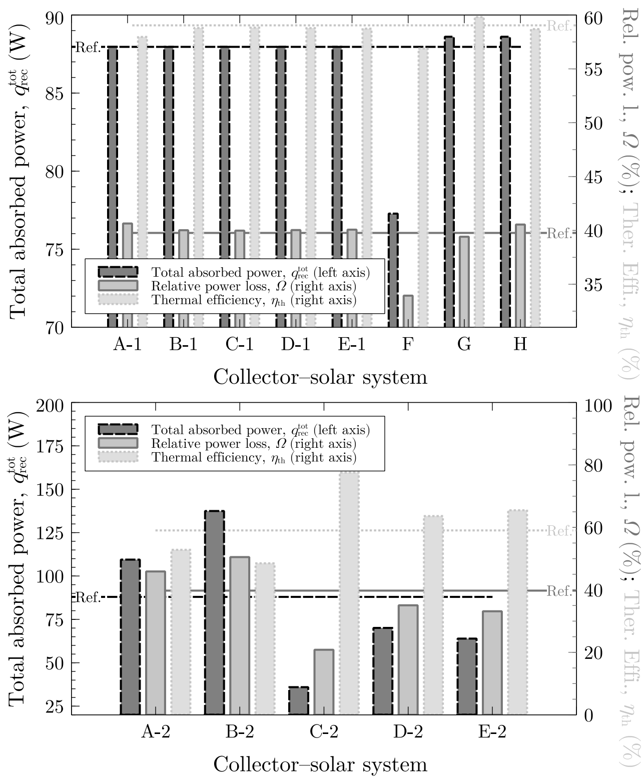

Fig. 13. Total solar absorbed power, relevance of heat (re-emission) losses in relation to the total absorbed power, and thermal efficiency for systems of similar receiver power-on-aperture (a) and systems of equal solar flux value at the concentrator aperture (b).

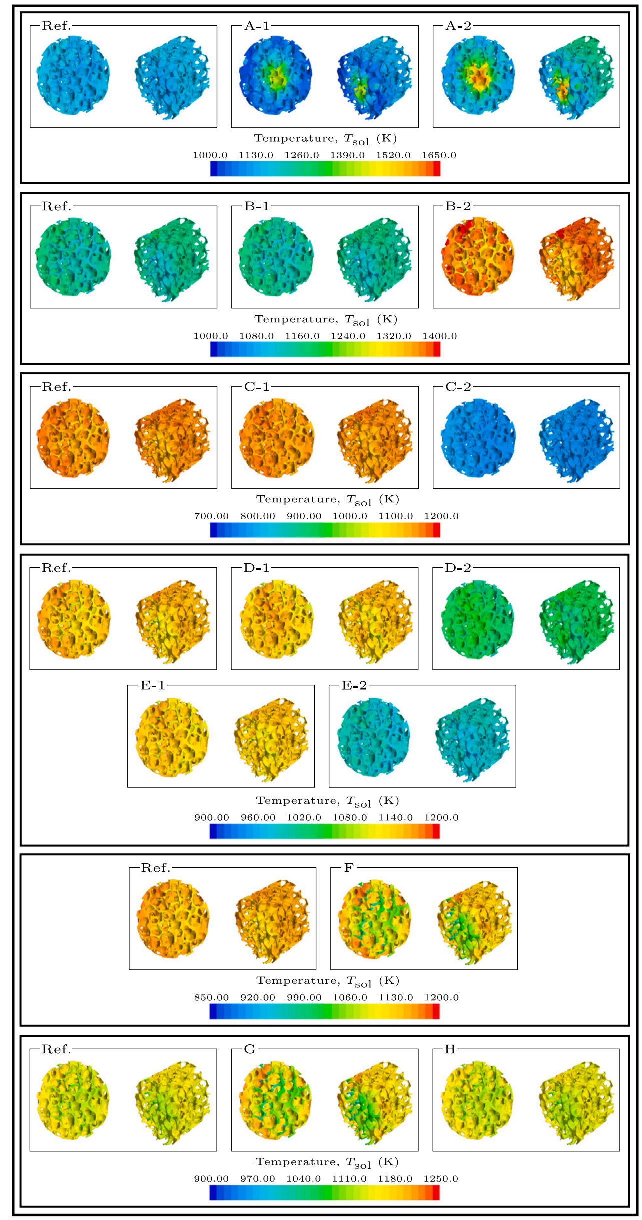

Fig. 14. Absorber surface temperature distributions for each collector–solar system.

of the total absorbed power that is lost by radiative emission from the receiver unit to the surroundings —, and the collector solar-to-thermal energy conversion efficiency — shortly, thermal efficiency (η_{th}) — for each system. The relative emission losses and the thermal efficiency are computed according to Eqs. (27) and (28), respectively. In Eqs. (27)–(28), $q_{rec,loss}$ and q_{gas} $\left(\equiv q_{rec}^{tot} - q_{rec,loss}\right)$ are the total radiative power loss from the receiver unit to the external surroundings and the total power transferred to the heat transfer fluid by convective heat transfer between the receiver inlet and outlet sections, respectively. (The thermal efficiency is also given by the product $\epsilon_{ap}\,(1-\Omega)$.)

$$\Omega = \frac{q_{rec,loss}}{q_{rec}^{tot}} \tag{27}$$

$$\eta_{th} = \frac{q_{gas}}{q_{rec}^{aper}} \tag{28}$$

Fig. 14 presents absorber surface temperatures for each system. (For clarity, distinct temperature intervals are considered for different sets of systems.)

Figs. 15(a)–(b) present absolute temperature differences between the values observed for each system and the values registered for the reference system. For ease of visualization, Figs. 13(a) and 15(a) consider systems featuring a similar receiver power-on-aperture value (about 90 W) — Systems Y-1, F, G, and H —, while Figs. 13(b) and 15(b) consider systems with an equal solar flux value at the concentrator aperture (Systems Y-2).

According to Fig. 13(a), Systems A-1 to E-1 exhibit higher power losses than the reference system. Thus, the power transferred to the heat transfer fluid is lower for Systems A-1 to E-1 than for the reference system. Since the apparent emissivity value is similar for Systems A-1 to E-1 and for the reference system (see Fig. 11), the thermal efficiency for Systems A-1 to E-1 is lower than the thermal efficiency observed for the reference system.

Particularly for System A-1, the concentration of solar radiation observed at the central portion of the irradiated absorber section (see Fig. 10) leads to a local high temperature region (local overheating) which contributes to an increase in radiative heat losses in relation to the reference system — note that the maximum absorber temperature for System A-1 is about 300 K higher than for the reference system (see Figs. 14 and 15(a)). However, it is worth noting that a small decrease in the concentrator focal length from the reference value keeping constant the total absorber power by the receiver unit may not result in a meaningful difference on the receiver hydrothermal performance. This is true provided that the decrease is sufficiently small such that optical spillage losses remain present, thereby ensuring a relatively uniform concentrated solar flux distribution across the receiver aperture section — see Figs. 3(a) and 4(b) according to which a decrease in the focal length (*i.e.*, an increase in the rim angle) reduces the size of the central core region (r_{core} decreases) while maintaining an approximately constant solar flux within this region.

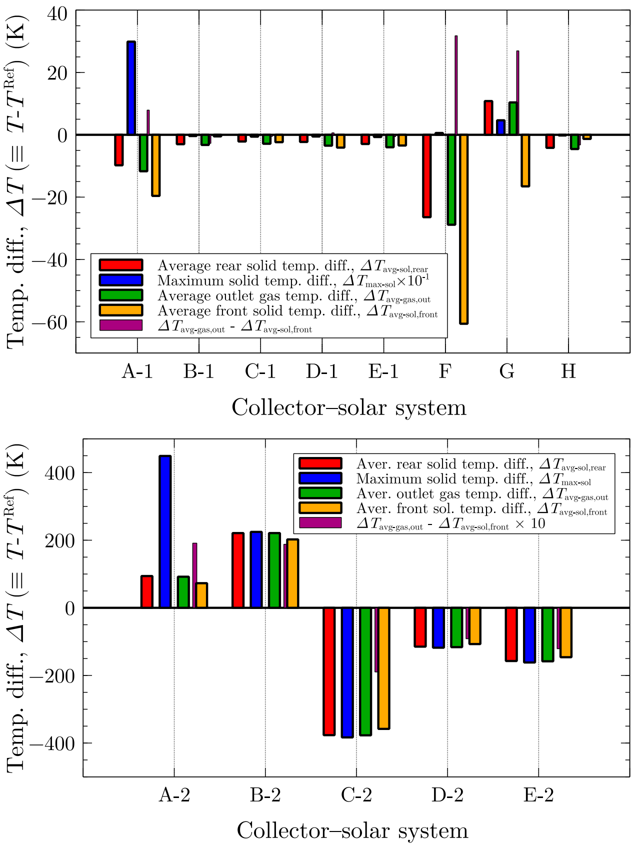

Fig. 15. Temperature differences between each collector–solar system and the reference system: (a) systems of similar receiver power-on-aperture; and (b) systems of equal solar flux value at the concentrator aperture. For the reference system, the average rear solid temperature is 1153.6 K, the maximum solid temperature is 1169.7 K, the average outlet gas temperature is 1152.7 K, and the average front solid temperature is 1132.4 K.

The lower power values transferred to the heat transfer fluid for Systems A-1 to E-1 in relation to the value registered for the reference system are in full agreement with the lower outlet gas temperatures for Systems A-1 to E-1 that are observed in Fig. 15(a) ($\Delta T_{\mathrm{avg-gas,out}} < 0$). The thermal performance of systems B-1 and C-1 is much more similar to the performance of the reference system than the performance of system A-1, D-1 and E-1, as it can be concluded in Figs. 14 and 15(a) and by comparable relative power loss and thermal efficiency values in Fig. 13(a). The results for system B-1 in relation to the reference system results suggest that the incident solar radiation angle plays a minor (less relevant) role on the receiver thermal performance. This conclusion is in agreement with past research [36] that applied a continuum approach — not discrete as in this work — for MCRT model simulations of concentrated solar radiation transport along the absorber structure.

Regarding Systems Y-2, particularly, in the case of System B-2, a concentrator aperture radius equal to 0.25 m was considered — rather than the value considered for System B-1 — to avoid excessive and physically unrealistic temperatures.

Considering a constant DNI value (reference and Y-2 systems), Fig. 13(b) shows that the total absorbed power increases by decreasing the concentrator focal length or increasing the concentrator aperture radius and decreases upon increasing the concentrator surface slope error or the collector axial alignment error. These trends are in agreement — and could be anticipated — with the solar flux values at the concentrator surfaces required for systems A-1 to E-1 to keep the total absorbed solar power constant and equal to the reference system (see the last row of Table 2). The increase of the total absorbed power upon decreasing the focal length is due to a reduction of optical spillage losses — see Fig. 11. Increasing the concentrator aperture area increases the power collected and reflected by the concentrator and, consequently, the power absorbed by the receiver unit even though the optical spillage loss factor increases — see Fig. 11. The increase of the concentrator surface slope error or collector axial alignment error leads to an increase of optical spillage losses and a reduction of the total absorbed power. Reducing the focal length not only increases the total absorbed power, but also concentrates the focal spot towards the center of the absorber, resulting in a highly non-uniform solar flux distribution at the receiver aperture, and consequently across the internal surfaces of the receiver — see Fig. 10. On the other hand, an increase in the concentrator aperture radius, surface slope error, or axial alignment error primarily affects the total absorbed power, while preserving a relatively uniform flux distributions at the receiver aperture.

Since the receiver unit (and its operating conditions) as well as the solar system definitions (DNI) are the same for the concentrating collector systems under consideration, a concentrator parameter change promoting an increase in the total absorbed power leads to an increase in the relative heat losses and a decrease in the thermal efficiency, even though the power transferred to the heat transfer fluid is higher (higher outlet fluid temperatures — see Fig. 15(b)).

For the same concentrating collector system, an increase in the solar flux irradiation (DNI) leads to a simultaneous increase in the total absorbed power, relative heat losses, and receiver temperatures (compare systems Y-1 and Y-2 in Figs. 13(a), 15(a), 13(b), and 15(b)). The thermal efficiency decreases as the solar flux irradiation increases because the heat losses — driven by radiative (re-emission) heat transfer — become more relevant at higher temperatures. Nevertheless, it is noteworthy that an increase of the solar flux irradiation may still represent an opportunity to increase the collector thermal efficiency if the receiver hydrodynamic and thermal operating conditions were adjusted accordingly — for instance, if a higher heat transfer fluid mass flow rate were fed into the receiver.

Regarding the hydrothermal performance obtained for different absorber and coating materials, Fig. 13(a) shows that an uncoated alumina absorber leads to a lower total absorbed power in relation to an uncoated SiC absorber — as could be anticipated by the corresponding apparent emissivity values. Strikingly, alumina features a more efficient conversion of absorbed power into useful power than for SiC. An uncoated alumina absorber (System F) dissipates approximately 6 percentage points less power per unit of absorbed power compared to an uncoated SiC absorber (reference system). For the same total absorbed power observed for Systems G and H (Pyromark-coated foams), alumina allows a more energy conversion efficient operation than silicon carbide. Consequently, a Pyromark-coated alumina absorber shows a higher thermal efficiency than Pyromark-coated SiC absorber. The improved energy conversion efficiency provided by alumina absorbers is due to the lower thermal conductivity of the absorber material that prevents the heat transfer from the internal walls towards the absorber entrance surfaces that are directly exposed to the upstream ambient environment.

Despite exhibiting lower relative heat losses, the uncoated alumina absorber (System F) delivers less power to the heat transfer fluid due to its substantially lower total absorbed solar power compared to the reference case. As a result, System F attains a lower outlet gas temperature and thermal efficiency than the reference system (see Fig. 15(a)). In contrast, the Pyromark-coated alumina absorber (System G) achieves both higher total absorbed solar power and lower relative power losses. This combination leads to greater useful power output and, consequently, a higher outlet fluid temperature and thermal efficiency values than those of the reference system (see Figs. 13(a) and 15(a)).

Fig. 15(a) shows that for Systems F and G the difference between the average outlet gas temperature and the average front solid temperature is even higher than such a difference observed for the reference system ($\Delta T_{\text{avg-gas,out}} - \Delta T_{\text{avg-sol,front}} > 0$). These results indicate that the volumetric effect — commonly assumed present when the ratio $T_{\text{avg-gas,out}}/T_{\text{avg-sol,front}} > 1$ [12,74] — becomes more pronounced with an alumina absorber. (The ratio $T_{\text{avg-gas,out}}/T_{\text{avg-sol,front}}$ is approximately equal 1.05 and 1.04 for System F and System G, respectively, and about 1.02 for the reference system.) System F presents simultaneously an enhanced volumetric effect and a lower thermal efficiency in comparison with the reference case. This outcome is consistent with previous studies showing that enhancing the volumetric effect does not necessarily translate into higher receiver thermal efficiency [12, 75]. The volumetric effect and the thermal efficiency are independent volumetric solar absorber parameters.

The volumetric effect in a volumetric solar absorber is considered to occur when the actual (measured) radiative power loss from the receiver (through the front section towards the surroundings) is lower than the radiative power loss that would result if the receiver surfaces were at the (average) outlet gas temperature. The ratio $T_{\text{avg-gas,out}}/T_{\text{avg-sol,front}}$, commonly used in the literature to assess the presence of the volumetric effect, is generally a reliable indicator. In this work, the volumetric effect was concluded to be present in all systems considered, as the ratio $T_{\text{avg-gas,out}}/T_{\text{avg-sol,front}}$ was greater than unity. However, for some systems the ratio is only marginally above one, which makes the assessment of volumetric effect less clear. This occurs, particularly, for System C-2 due to a negligible temperature difference of about 2 K between the average outlet gas temperature and the average front solid temperature.

Fig. 16 presents the radiative power loss observed for SiC, Al_2O_3, and Pyromark-coated foams for different effective receiver surface temperatures — all receiver surfaces were at the same (effective) temperature.

In Fig. 16, each solar–collector system under consideration is presented as a point (represented by a symbol) stating the corresponding actual values for the average gas temperature at the outlet section and the radiative power loss. Since each point is located below the line that represents the corresponding absorber material/coating — *i.e.,* the actual power loss is lower than the power loss that would be observed for a similar receiver with an effective temperature equal to the average outlet gas temperature —, all systems verify the presence of the volumetric effect. The most expressive volumetric effect extent is observed for Systems F, G, and B-2 — these systems lose approximately 21.3%, 19.4%, and 17.4%, respectively, less power than the power they would lose if their surfaces were at the corresponding average outlet gas temperature. The volumetric effect is less expressive for Systems E-2, D-2, and A-1 with, respectively, 8.2%, 9.6%, and 10.3% lower power losses in relation to the power losses that would be observe if the corresponding surfaces were at the corresponding average outlet gas temperatures.

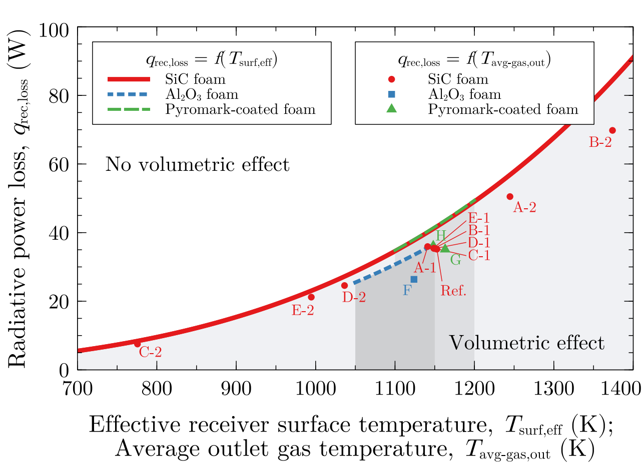

Fig. 16. Operating regimes for SiC, Al_2O_3, and Pyromark-coated foams, with shaded regions indicating the presence of the volumetric effect. Each symbol represents a specific solar–collector system.

Alumina is not recognized as a primary choice for the absorber material — as SiC commonly is — mainly because of its weak solar absorptivity. However, the results show that the thermal conductivity of alumina is more appropriate to prevent heat losses than that of SiC. According to the results of system G, absorber materials with a higher solar absorptivity (thermal emissivity) and a lower thermal conductivity have benefits on every performance indicator herein analyzed — total absorbed power, relative power loss, average outlet gas temperature, and optical and thermal efficiencies, and the presence of an expressive volumetric effect. Nevertheless, other technical parameters come naturally into play for the selection of a suitable absorber material which were not addressed in this study, namely those related with the structure mechanical and material chemical stabilities that become relevant to ensure a receiver long service life with minimal maintenance assistance while operating at high performance standards.

5.2.3. Global system performance

The overall (global) collector efficiency allows to simultaneously take into the collector optical and thermal performance. The overall efficiency is computed according to Eq. (29). (The overall efficiency is also given by the product $\rho_{\text{conc}}\left(1 - \alpha_{\text{spill}}\right)\eta_{\text{th}}$.)

$$\eta_o \equiv \frac{q_{\text{gas}}}{q_s'' A_{\text{aper}}} = \eta_{\text{op}(1-\Omega)} \tag{29}$$

Fig. 17 presents the overall collector efficiency for each collector–solar system under consideration.

The overall efficiency is governed by a sensitive balance between geometrical concentration, optical quality, and material response, rather than by any single parameter in isolation. Although reducing the focal length (Systems A-1 and A-2) yields the highest overall efficiency values, outperforming the reference system value, this apparent improvement must be interpreted cautiously: the increased concentration can intensify local heat flux peaks, potentially promoting localized overheating and accelerating the thermo-mechanical degradation of the ceramic foam. The increased overall efficiency values registered for Systems A-1 and A-2 in relation to the reference value were observed due to the relevant increase in the optical efficiency for such systems in relation to the optical efficiency registered for the reference system — see Fig. 17. In contrast, an increase in the concentrator aperture radius (Systems B-1 and B-2), concentrator surface slope error (Systems C-1 and C-2), and collector axial alignment error (Systems D-1/E-1 and D-2/E-2) results in poorer overall performance, mainly due to optical spillage that strongly penalizes the optical efficiency in these cases.

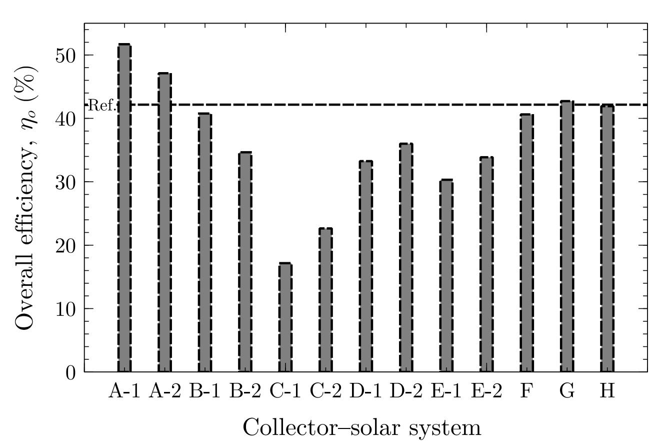

Fig. 17. Overall efficiency for each collector–solar system.

Moreover, when comparing Systems C-1/D-1/E-1 with Systems C-2/D-2/E-2, a higher overall efficiency is observed for the latter systems due to lower relative power losses, which result from the lower total absorbed power. Systems A-1 and B-1 present higher overall efficiency values than A-2 and B-1, respectively, mainly because Systems A-2 and B-2 present higher relative power losses than Systems A-1 and B-1, respectively. (The optical efficiency for System B-2 is slightly higher than that for System B-1 (70.01% *vs.* 67.96%) but such higher value is not sufficient to compensate the higher relative power losses observed for System B-2, and consequently, System B-2 has a lower overall thermal efficiency than System B-1.)

With respect to absorber materials and Pyromark coating application, replacing SiC (reference system) with Al_2O_3 (System F) results in a slight decrease in overall efficiency driven by the reduction observed in thermal efficiency — note that the spillage loss factor is independent of the receiver material and coating, and consequently, the overall efficiency varies in accordance to the variation of thermal efficiency. Applying a Pyromark coating onto the surfaces of a SiC foam absorber (System H) or a Al_2O_3 foam absorber (System F) leads to an increase in overall efficiency. Among the different combinations of absorber materials with or without coating application, the Pyromark-coated Al_2O_3 foam (System F) shows the highest overall efficiency.

Altogether, the results demonstrate that the system performance is strongly sensitive to the optical quality of the concentrating system, but also that the configurations delivering the highest overall efficiency may not necessarily represent the most robust or durable operating condition.

6. Conclusions and final remarks

This study applies a fully coupled pore-scale modeling framework that integrates Monte Carlo ray tracing with direct hydrothermal simulations on reconstructed ceramic foams – acquired by computed tomography scans – to evaluate the performance of parabolic dish concentrator equipped with an open volumetric receiver. By resolving radiation transport, absorption, fluid flow, and conjugate heat transfer directly within the real porous geometry, the applied methodology eliminates reliance on empirical closure correlations and provides detailed physical insight into the coupled thermo-optical behaviour of the volumetric receiver.

The results demonstrate that concentrator geometrical and optical parameters strongly govern the spatial distribution of concentrated solar flux and, consequently, receiver thermal performance. Higher rim angles generate more compact and intense focal spots but widen the incidence angle distribution and produce peripheral flux tails. Small axial misalignments ($\delta_f/f \approx 0.006$–0.008) significantly deteriorate flux uniformity and increase spillage losses, while surface slope errors broaden the focal region and reduce optical efficiency. These findings highlight the importance of stringent alignment and reflector surface quality in maintaining high optical performance.

At the receiver level, a clear trade-off between optical concentration and thermal efficiency was identified. Lower focal lengths increase absorbed power but intensify non-uniform heating, elevating local solid temperatures and radiative losses. Similarly, increasing the aperture radius also leads to higher absorbed power, but it does not necessarily result in more pronounced non-uniform heating. Importantly, stronger volumetric heating ($T_{\text{gas,out}}/T_{\text{sol,in}} > 1$) does not necessarily translate into higher thermal efficiency.

Absorber material analysis reveals that thermal conductivity plays a critical role in performance optimization. Although SiC foam exhibits higher intrinsic absorptivity, Pyromark-coated alumina foam demonstrate superior conversion of absorbed power into useful thermal output due to reduced heat conduction towards exposed surfaces. The combination of high absorptivity and low conductivity, achieved with Pyromark-coated alumina, provides the best overall performance, yielding higher outlet temperatures and improved thermal efficiency. These results emphasize that maximizing solar absorption alone is insufficient. Therefore, optimal design requires balancing absorptivity, thermal conductivity, and flux distribution.

Overall, the study identifies key design trade-offs governing high-temperature volumetric receivers and provides quantitative guidance for optimizing concentrator geometry, material selection, and operating conditions. The developed framework offers a robust tool for advancing next-generation concentrated solar power systems capable of delivering high-temperature heat for dispatchable electricity generation and industrial process applications.

CRediT authorship contribution statement

Leonardo F. Martins: Writing – review & editing, Writing – original draft, Visualization, Validation, Investigation, Conceptualization. **Jorge E.P. Navalho:** Writing – review & editing, Writing – original draft, Visualization, Validation, Software, Methodology, Investigation, Conceptualization. **Miguel A.A. Mendes:** Writing – review & editing. **José C.F. Pereira:** Writing – review & editing, Resources, Funding acquisition.

Declaration of competing interest

The authors declare that they have no known competing financial interests or personal relationships that could have appeared to influence the work reported in this paper.

Acknowledgments

The authors acknowledge Fundação para a Ciência e a Tecnologia (FCT), Portugal for its financial support via the projects LAETA Base Funding (DOI: 10.54499/UIDB/50022/2020) and LAETA Programmatic Funding (DOI: 10.54499/UIDP/50022/2020).

Jorge E. P. Navalho acknowledges financial support via national funds from FCT, I.P. - Fundação para a Ciência e a Tecnologia, Portugal financed this work in the scope of the project UID/00667/2025 (UNIDEMI).

Data availability

Data will be made available on request.

References

[1] Masson-Delmotte V, Zhai P, Chen Y, Goldfarb L, Gomis MI, Matthews JBR, Berger S, Huang M, Yelekçi O, Yu R, Zhou B, Lonnoy E, Maycock TK, Waterfield T, Leitzell K, Caud N. The physical science basis summary for policymakers technical summary frequently asked questions glossary part of the working group I contribution to the sixth assessment report of the intergovernmental panel on climate change edited by. 2021.

[2] Khan MI, Gutiérrez-Alvarez R, Asfand F, Bicer Y, Sgouridis S, Al-Ghamdi SG, Jouhara H, Asif M, Kurniawan TA, Abid M, Pesyridis A, Farooq M. The economics of concentrating solar power (CSP): Assessing cost competitiveness and deployment potential. 2024, http://dx.doi.org/10.1016/j.rser.2024.114551.

[3] Navalho JE, Pereira JC. A comprehensive and fully predictive discrete methodology for volumetric solar receivers: application to a functional parabolic dish solar collector system. Appl Energy 2020;267. http://dx.doi.org/10.1016/j.apenergy.2020.114781.

[4] Pal RK, K. RK. Investigations of thermo-hydrodynamics, structural stability, and thermal energy storage for direct steam generation in parabolic trough solar collector: A comprehensive review. 2021, http://dx.doi.org/10.1016/j.jclepro.2021.127550.

[5] Abed AA, El-Marghany MR, El-Awady WM, Hamed AM. Recent advances in parabolic dish solar concentrators: Receiver design, heat loss reduction, and nanofluid optimization for enhanced efficiency and applications. 2024, http://dx.doi.org/10.1016/j.solmat.2024.112930.

[6] Ávila-Marín AL. Volumetric receivers in solar thermal power plants with central receiver system technology: A review. Sol Energy 2011;85:891–910. http://dx.doi.org/10.1016/j.solener.2011.02.002.

[7] He YL, Du S, Shen S. Advances in porous volumetric solar receivers and enhancement of volumetric absorption. 2023, http://dx.doi.org/10.1016/j.enrev.2023.100035.
[8] Dai G, Liu Y, Chen X, Zhao T. Optimization of heat transfer performances within porous solar receivers—A comprehensive review. 2025, http://dx.doi.org/10.3390/en18051201.
[9] García-Ferrero J, Corral RPM, Moctezuma-Hernández JA, Pérez-Gallego D, Anvari S, González-Ayala J, Calvo-Hernández A, Roco JMM, Santos MJ, Medina A. Parabolic dish collectors for concentrated solar power: A comprehensive review on their subsystems and overall integration. 2025, http://dx.doi.org/10.3390/en18246596.
[10] Barreto G, Canhoto P, Collares-Pereira M. Three-dimensional CFD modelling and thermal performance analysis of porous volumetric receivers coupled to solar concentration systems. Appl Energy 2019;252. http://dx.doi.org/10.1016/j.apenergy.2019.113433.
[11] Gomez-Garcia F, González-Aguilar J, Olalde G, Romero M. Thermal and hydrodynamic behavior of ceramic volumetric absorbers for central receiver solar power plants: A review. 2016, http://dx.doi.org/10.1016/j.rser.2015.12.106.
[12] Luque S, Menéndez G, Roccabruna M, González-Aguilar J, Crema L, Romero M. Exploiting volumetric effects in novel additively manufactured open solar receivers. Sol Energy 2018;174:342–51. http://dx.doi.org/10.1016/j.solener.2018.09.030.
[13] Muñoz M, Rovira A, Montes MJ. Thermodynamic cycles for solar thermal power plants: A review. 2022, http://dx.doi.org/10.1002/wene.420.
[14] Wang P, Li JB, Zhou L, Vafai K. Experimental characterization on pore parameter and the irradiation absorption efficiency of a series SiC foam specimens. Energy Convers Manage 2020;212. http://dx.doi.org/10.1016/j.enconman.2020.112795.
[15] Wang P, Li JB, Xu RN, Jiang PX. Non-uniform and volumetric effect on the hydrodynamic and thermal characteristic in a unit solar absorber. Energy 2021;225. http://dx.doi.org/10.1016/j.energy.2021.120130.
[16] Li T, Xie L, Zhao B, Shen W, Liu Y. Analysis on the effects of different receiver structures and porous parameters on the volumetric effects and heat transfer performance of porous volumetric solar receiver. Int J Energy Res 2023;2023. http://dx.doi.org/10.1155/2023/3289428.
[17] Barreto G, Canhoto P, Collares-Pereira M. Parametric analysis and optimisation of porous volumetric solar receivers made of open-cell SiC ceramic foam. Energy 2020;200. http://dx.doi.org/10.1016/j.energy.2020.117476.
[18] Zhu Q, Xuan Y. Pore scale numerical simulation of heat transfer and flow in porous volumetric solar receivers. Appl Therm Eng 2017;120:150–9. http://dx.doi.org/10.1016/j.applthermaleng.2017.03.141.
[19] Du S, Li MJ, He Y, Li ZY. Experimental and numerical study on the reflectance losses of the porous volumetric solar receiver. Sol Energy Mater Sol Cells 2020;214. http://dx.doi.org/10.1016/j.solmat.2020.110558.
[20] Du S, He YL, Yang WW, Liu ZB. Optimization method for the porous volumetric solar receiver coupling genetic algorithm and heat transfer analysis. Int J Heat Mass Transfer 2018;122:383–90. http://dx.doi.org/10.1016/j.ijheatmasstransfer.2018.01.120.
[21] Du S, Li MJ, Ren Q, Liang Q, He YL. Pore-scale numerical simulation of fully coupled heat transfer process in porous volumetric solar receiver. Energy 2017;140:1267–75. http://dx.doi.org/10.1016/j.energy.2017.08.062.
[22] Du S, Li D, Li MJ, He YL. Numerical investigation on the flow and thermal behaviors of the volumetric solar receivers with different morphologies. Sci China Technol Sci 2024;67:2749–57. http://dx.doi.org/10.1007/s11431-024-2635-9.
[23] Caliot C, Déjardin PM. Numerical demonstration of the volumetric effect in a high specific surface absorber with kelvin cells. In: AIP conference proceedings. vol. 2126, American Institute of Physics Inc.; 2019, http://dx.doi.org/10.1063/1.5117523.
[24] Wang P, Li JB, Bai FW, Liu DY, Xu C, Zhao L, Wang ZF. Experimental and theoretical evaluation on the thermal performance of a windowed volumetric solar receiver. Energy 2017;119:652–61. http://dx.doi.org/10.1016/j.energy.2016.11.024.
[25] Wang F, Tan J, Yong S, Tan H, Chu S. Thermal performance analyses of porous media solar receiver with different irradiative transfer models. Int J Heat Mass Transfer 2014;78:7–16. http://dx.doi.org/10.1016/j.ijheatmasstransfer.2014.06.035.
[26] Villafán-Vidales HI, Abanades S, Caliot C, Romero-Paredes H. Heat transfer simulation in a thermochemical solar reactor based on a volumetric porous receiver. Appl Therm Eng 2011;31:3377–86. http://dx.doi.org/10.1016/j.applthermaleng.2011.06.022.
[27] Wu Z, Caliot C, Flamant G, Wang Z. Coupled radiation and flow modeling in ceramic foam volumetric solar air receivers. Sol Energy 2011;85:2374–85. http://dx.doi.org/10.1016/j.solener.2011.06.030.
[28] Nakakura M, Bellan S, Matsubara K, Kodama T. Conjugate radiation-convection-conduction simulation of volumetric solar receivers with cut-back inlets. Sol Energy 2018;170:606–17. http://dx.doi.org/10.1016/j.solener.2018.06.006.
[29] Faizan M, Almerbati A, Yilbas BS. A novel approach for volumetric solar receiver performance assessments. Appl Therm Eng 2022;211. http://dx.doi.org/10.1016/j.applthermaleng.2022.118487.
[30] Sanchez-Señoran D, Reyes-Belmonte MA, Kinzel MP, Casanova M, Avila-Marin AL. Geometrical comparison of inline and staggered stack wire mesh absorbers for solar volumetric receivers. Case Stud Therm Eng 2025;66. http://dx.doi.org/10.1016/j.csite.2024.105729.
[31] Argentot C, Bouvardt D. A ray tracing method for evaluating the radiative heat transfer in porous media. Tech. rep., 1996.
[32] Tancrez M, Taine J. Direct identification of absorption and scattering coefficients and phase function of a porous medium by a Monte Carlo technique. Int J Heat Mass Transfer 2004;47:373–83. http://dx.doi.org/10.1016/S0017-9310(03)00146-7.
[33] Petrasch J, Wyss P, Steinfeld A. Tomography-based Monte Carlo determination of radiative properties of reticulate porous ceramics. J Quant Spectrosc Radiat Transfer 2007;105:180–97. http://dx.doi.org/10.1016/j.jqsrt.2006.11.002.
[34] Brunser SS, Steinfeld A. Design and optimization of hierarchically ordered porous structures for solar thermochemical fuel production using a voxel-based Monte Carlo ray-tracing algorithm. ACS Eng Au 2023;3:326–34. http://dx.doi.org/10.1021/acsengineeringau.3c00013.
[35] Brantley PS, Gentile NA, Zimmerman GB. Beyond levermore-pomraning for implicit Monte Carlo radiative transfer in binary stochastic media. Tech. rep..
[36] Chen X, Xia XL, Liu H, Li Y, Liu B. Heat transfer analysis of a volumetric solar receiver by coupling the solar radiation transport and internal heat transfer. Energy Convers Manage 2016;114:20–7. http://dx.doi.org/10.1016/j.enconman.2016.01.074.
[37] Heisig LM, Markuske K, Werzner E, Wulf R, Fieback TM. Experimental and simplified predictive determination of extinction coefficients of ceramic open-cell foams used for metal melt filtration. Adv Eng Mater 2022;24. http://dx.doi.org/10.1002/adem.202100723.
[38] Chen X, Xia XL, Dong XH, Dai GL. Integrated analysis on the volumetric absorption characteristics and optical performance for a porous media receiver. Energy Convers Manage 2015;105:562–9. http://dx.doi.org/10.1016/j.enconman.2015.08.028.
[39] Cui FQ, He YL, Cheng ZD, Li D, Tao YB. Numerical simulations of the solar transmission process for a pressurized volumetric receiver. Energy 2012;46:618–28. http://dx.doi.org/10.1016/j.energy.2012.07.044.
[40] Bai F. One dimensional thermal analysis of silicon carbide ceramic foam used for solar air receiver. Int J Therm Sci 2010;49:2400–4. http://dx.doi.org/10.1016/j.ijthermalsci.2010.08.010.
[41] Lee HJ, Kim JK, Lee SN, Kang YH. Consistent heat transfer analysis for performance evaluation of multichannel solar absorbers. Sol Energy 2012;86:1576–85. http://dx.doi.org/10.1016/j.solener.2012.02.020.
[42] Kribus A, Gray Y, Grijnevich M, Mittelman G, Mey-Cloutier S, Caliot C. The promise and challenge of solar volumetric absorbers. Sol Energy 2014;110:463–81. http://dx.doi.org/10.1016/j.solener.2014.09.035.
[43] Zaversky F, Aldaz L, Sánchez M, Ávila-Marín AL, Roldán MI, Fernández-Reche J, Füssel A, Beckert W, Adler J. Numerical and experimental evaluation and optimization of ceramic foam as solar absorber – Single-layer vs multi-layer configurations. Appl Energy 2018;210:351–75. http://dx.doi.org/10.1016/j.apenergy.2017.11.003.
[44] Avila-Marin AL, Fernandez-Reche J, Martinez-Tarifa A. Modelling strategies for porous structures as solar receivers in central receiver systems: A review. -2019, http://dx.doi.org/10.1016/j.rser.2019.03.059.
[45] Chen X, Lyu J, Sun C, Xia X, Wang F. Pore-scale evaluation on a volumetric solar receiver with different optical property control strategies. Energy 2023;278. http://dx.doi.org/10.1016/j.energy.2023.128006.
[46] Avila-Marin AL, Caliot C, de Lara MA, Fernandez-Reche J, Montes MJ, Martinez-Tarifa A. Homogeneous equivalent model coupled with P1-approximation for dense wire meshes volumetric air receivers. Renew Energy 2019;135:908–19. http://dx.doi.org/10.1016/j.renene.2018.12.061.
[47] Navalho JE, Silva LG, Pereira JC. An investigation on the thermal performance of volumetric solar absorbers with lateral wall power losses. Sol Energy 2024;282. http://dx.doi.org/10.1016/j.solener.2024.112937.
[48] Navalho JE, Pereira JC. Investigating the impact of modeling assumptions and closure models on the steady-state prediction of solar-driven methane steam reforming in a porous reactor. Energy Convers Manage 2023;295. http://dx.doi.org/10.1016/j.enconman.2023.117577.
[49] Li Z, Xia X, Li X, Sun C. Discrete vs. continuum-scale simulation of coupled radiation and convection inside rectangular channel filled with metal foam. Int J Therm Sci 2018;132:219–33. http://dx.doi.org/10.1016/j.ijthermalsci.2018.06.010.
[50] Sepehri E, Siavashi M. Pore-scale direct numerical simulation of fluid dynamics, conduction and convection heat transfer in open-cell voronoi porous foams. Int Commun Heat Mass Transfer 2022;137. http://dx.doi.org/10.1016/j.icheatmasstransfer.2022.106274.
[51] de Carvalho TP, Morvan HP, Hargreaves DM, Oun H, Kennedy A. Pore-scale numerical investigation of pressure drop behaviour across open-cell metal foams. Transp Porous Media 2017;117:311–36. http://dx.doi.org/10.1007/s11242-017-0835-y.
[52] Du S, Tong ZX, Zhang HH, He YL. Tomography-based determination of nusselt number correlation for the porous volumetric solar receiver with different geometrical parameters. Renew Energy 2019;135:711–8. http://dx.doi.org/10.1016/j.renene.2018.12.001.

[53] Du S, He Y, Li D, Liu Z, Li M. Comparison of direct pore-scale and volume-averaging methods for the performance evaluation of porous volumetric solar receiver. J Therm Sci 2024;33:1607–17. http://dx.doi.org/10.1007/s11630-024-2019-8.

[54] Sedighi M, Taylor RA, Padilla RV. Experimentally validated pore-scale numerical analysis for high-temperature (>700° c), high-efficiency (>90 receivers. Energy Convers Manag: X 2021;12. http://dx.doi.org/10.1016/j.ecmx.2021.100127.

[55] Bekele EA, Ancha VR, Binchebo TL. Analysis of solar irradiance variation on heat flux and temperature distribution for a dish concentrator receiver. ASME Open J Eng 2022;1. http://dx.doi.org/10.1115/1.4053963.

[56] Hafez AZ, Soliman A, El-Metwally KA, Ismail IM. Design analysis factors and specifications of solar dish technologies for different systems and applications. 2017, http://dx.doi.org/10.1016/j.rser.2016.09.077.

[57] Yushkevich PA, Piven J, Hazlett HC, Smith RG, Ho S, Gee JC, Gerig G. User-guided 3D active contour segmentation of anatomical structures: Significantly improved efficiency and reliability. NeuroImage 2006;31:1116–28. http://dx.doi.org/10.1016/j.neuroimage.2006.01.015.

[58] Blanc P, Espinar B, Geuder N, Gueymard C, Meyer R, Pitz-Paal R, Reinhardt B, Renné D, Sengupta M, Wald L, Wilbert S. Direct normal irradiance related definitions and applications: The circumsolar issue. Sol Energy 2014;110:561–77. http://dx.doi.org/10.1016/j.solener.2014.10.001.

[59] Foulaadvand ME, Aghamohammadi A, Karimi P, Borzouei H. Flux profile at focal area of concentrating solar dishes. Sci Rep 2021;11. http://dx.doi.org/10.1038/s41598-021-03768-w.

[60] Zou B, Dong J, Yao Y, Jiang Y. A detailed study on the optical performance of parabolic trough solar collectors with Monte Carlo ray tracing method based on theoretical analysis. Sol Energy 2017;147:189–201. http://dx.doi.org/10.1016/j.solener.2017.01.055.

[61] Cunsolo S, Oliviero M, Harris WM, Andreozzi A, Bianco N, Chiu WK, Naso V. Monte Carlo determination of radiative properties of metal foams: Comparison between idealized and real cell structures. Int J Therm Sci 2015;87:94–102. http://dx.doi.org/10.1016/j.ijthermalsci.2014.08.006.

[62] Modest MF, Mazumder S. Radiative heat transfer. 3rd ed.. New York: Academic Press (Elsevier); 2013, p. 0–993.

[63] White FM. Fluid mechanics. 4th ed.. New York: McGraw-Hill Education; 1999.

[64] Munro RG. Material properties of a sintered α-SiC. J Phys Chem Ref Data 1997;26:1195–203. http://dx.doi.org/10.1063/1.556000.

[65] Munro RG. Evaluated material properties for a sintered α-alumina. 1997, http://dx.doi.org/10.1111/j.1151-2916.1997.tb03074.x.

[66] VDI-Gesellschaft Verfahrenstechnik und Chemieingenieurwesen, editor. VDI heat atlas. 2nd ed.. Berlin, Germany: Springer; 2010, http://dx.doi.org/10.1007/978-3-540-77877-6.

[67] Mao Q, Shuai Y, Yuan Y. Study on radiation flux of the receiver with a parabolic solar concentrator system. Energy Convers Manage 2014;84:1–6. http://dx.doi.org/10.1016/j.enconman.2014.03.083.

[68] Zhu Q, Xuan Y. Performance analysis of a volumetric receiver composed of packed shaped particles with spectrally dependent emissivity. Int J Heat Mass Transfer 2018;122:421–31. http://dx.doi.org/10.1016/j.ijheatmasstransfer.2018.02.006.

[69] Cunsolo S, Coquard R, Baillis D, Chiu WK, Bianco N. Radiative properties of irregular open cell solid foams. Int J Therm Sci 2017;117:77–89. http://dx.doi.org/10.1016/j.ijthermalsci.2017.03.007.

[70] Wen L, Huang L, Poon P, Carley W. Comparative study of solar optics for paraboloidal concentrators. J Sol Energy Eng 1980;102(4):305–15. http://dx.doi.org/10.1115/1.3266196.

[71] Chen X, Xia XL, Yan XW, Sun C. Heat transfer analysis of a volumetric solar receiver with composite porous structure. Energy Convers Manage 2017;136:262–9. http://dx.doi.org/10.1016/j.enconman.2017.01.018.

[72] Wang F, Guan Z, Tan J, Yan Z, Leng Y. Unsteady state thermochemical performance analyses of solar driven steam methane reforming in porous medium reactor. Sol Energy 2015;122:1180–92. http://dx.doi.org/10.1016/j.solener.2015.10.031.

[73] Fend T, Pitz-Paal R, Hoffschmidt B, Reutter O. Solar radiation conversion. In: Cellular ceramics: structure, manufacturing, properties and applications. Wiley Online Library; 2005, http://dx.doi.org/10.1002/3527606696.ch5g.

[74] Salih F, Kakosimos KE. Exploring and enhancing the volumetric behaviour in solar receivers through specular reflectivity and simplified design. Energy Convers Manage 2023;291:117306. http://dx.doi.org/10.1016/j.enconman.2023.117306, URL https://www.sciencedirect.com/science/article/pii/S0196890423006520.

[75] Cagnoli M, Savoldi L, Zanino R, Zaversky F. Coupled optical and CFD parametric analysis of an open volumetric air receiver of honeycomb type for central tower CSP plants. Sol Energy 2017;155:523–36. http://dx.doi.org/10.1016/j.solener.2017.06.038, URL https://www.sciencedirect.com/science/article/pii/S0038092X17305479.